Article

Molecular Cell

The Dynamics of Cytoplasmic mRNA Metabolism

Graphical Abstract

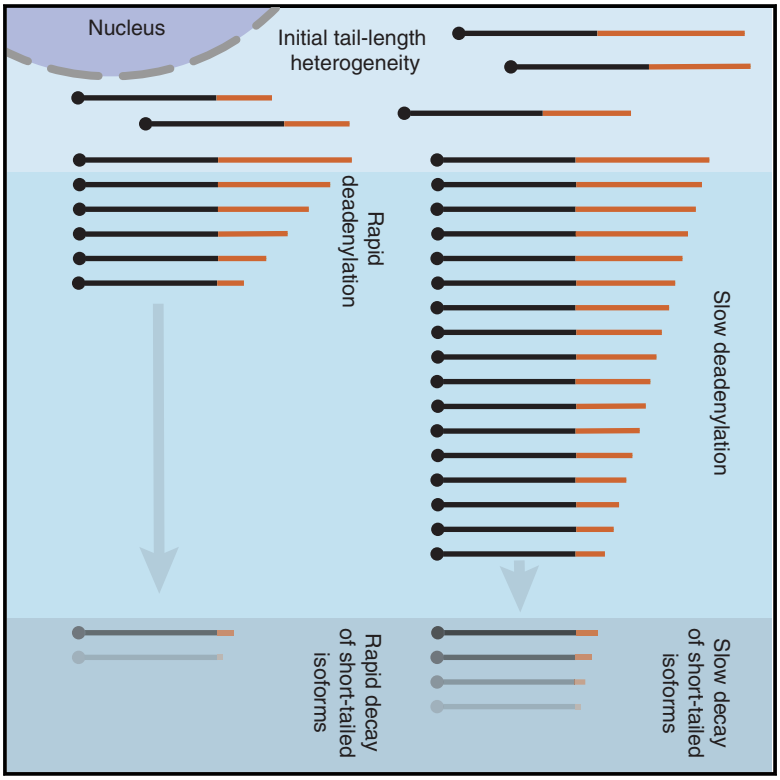

Highlights

- mRNAs enter the cytoplasm with diverse intra- and intergenic tail lengths
- mRNA deadenylation rates span a 1000-fold range and correspond to mRNA half-lives
- After their tails become short, mRNAs decay at rates that span a 1000-fold range
- More rapidly deadenylated mRNAs decay more rapidly upon reaching short tail lengths

Authors

Timothy J. Eisen, Stephen W. Eichhorn, Alexander O. Subtelny, Kathy S. Lin, Sean E. McGeary, Sumeet Gupta, David P. Bartel

Correspondence

dbartel@wi.mit.edu

In Brief

mRNA decay helps determine the extent of mRNA accumulation and ultimately the amount of protein produced. The dynamics of mRNA decay—involving tail-length shortening and then decay of the mRNA body—are largely unknown. Eisen et al. use high-throughput methods to uncover these dynamics for thousands of endogenous mRNAs.

Eisen et al., 2020, Molecular Cell 77, 786–799
February 20, 2020
https://doi.org/10.1016/j.molcel.2019.12.005

CellPress

CellPress

Molecular Cell
Article

The Dynamics of Cytoplasmic mRNA Metabolism

Timothy J. Eisen,[1,2,3,5] Stephen W. Eichhorn,[1,2,3,5] Alexander O. Subtelny,[1,2,3,5] Kathy S. Lin,[1,2,3,4] Sean E. McGeary,[1,2,3] Sumeet Gupta,[2] and David P. Bartel[1,2,3,6,*]

[1]Howard Hughes Medical Institute, Cambridge, MA 02142, USA
[2]Whitehead Institute for Biomedical Research, Cambridge, MA 02142, USA
[3]Department of Biology, Massachusetts Institute of Technology, Cambridge, MA 02139, USA
[4]Computational and Systems Biology Program, Massachusetts Institute of Technology, Cambridge, MA 02139, USA
[5]These authors contributed equally
[6]Lead Contact
*Correspondence: dbartel@wi.mit.edu
https://doi.org/10.1016/j.molcel.2019.12.005

SUMMARY

For all but a few mRNAs, the dynamics of metabolism are unknown. Here, we developed an experimental and analytical framework for examining these dynamics for mRNAs from thousands of genes. mRNAs of mouse fibroblasts exit the nucleus with diverse intragenic and intergenic poly(A)-tail lengths. Once in the cytoplasm, they have a broad (1000-fold) range of deadenylation rate constants, which correspond to cytoplasmic lifetimes. Indeed, with few exceptions, degradation appears to occur primarily through deadenylation-linked mechanisms, with little contribution from either endonucleolytic cleavage or deadenylation-independent decapping. Most mRNA molecules degrade only after their tail lengths fall below 25 nt. Decay rate constants of short-tailed mRNAs vary broadly (1000-fold) and are larger for short-tailed mRNAs that have previously undergone more rapid deadenylation. This coupling helps clear rapidly deadenylated mRNAs, enabling the large range in deadenylation rate constants to impart a similarly large range in stabilities.

INTRODUCTION

mRNAs corresponding to different genes are degraded at substantially different rates, with some mRNAs turning over in minutes and others persisting for days (Dölken et al., 2008). Different conditions or developmental contexts can modify these rates, resulting in the destabilization of previously stable mRNAs, or vice versa (Rabani et al., 2011). These rate changes influence the dynamics of mRNA accumulation and, ultimately, the steady-state abundance of mRNAs.

Many proteins that promote mammalian mRNA degradation also can recruit deadenylase complexes. These include Pumilio (Van Etten et al., 2012), SMG5/7 (Mühlemann and Lykke-Andersen, 2010), GW182 (Fabian et al., 2011), BTG/TOB factors (Mauxion et al., 2009), Roquin (Leppek et al., 2013), YTHDF2 (Du et al., 2016), and HuR, TTP, and other proteins that bind AU- and GU-rich elements (Vlasova-St Louis and Bohjanen, 2011; Fabian et al., 2013). That these diverse modifiers of mRNA stability converge on deadenylation suggests that differences in deadenylation rates might explain a substantial fraction of the variation observed in mRNA stability.

In the past, the dynamics of mRNA deadenylation have been examined on a gene-by-gene basis, involving pulsed expression and subsequent analysis of mRNA transcripts using RNase H to cleave the mRNA and RNA blots to probe for the poly(A)-tailed 3′ fragment. Because this procedure has been performed for only a handful of cellular mRNAs in yeast (Decker and Parker, 1993; Muhlrad et al., 1994; Hilgers et al., 2006) and mammals (Mercer and Wake, 1985; Wilson and Treisman, 1988; Shyu et al., 1991; Chen and Shyu, 1995; Gowrishankar et al., 2005), some fundamental questions, including the extent to which a global relationship exists between deadenylation rate and mRNA stability, have remained unanswered.

Here, we developed experimental and analytical tools for the global analysis of tail-length dynamics. Applying these tools to the mRNAs of cultured mouse fibroblasts generated a unique resource of initial cytoplasmic tail lengths, deadenylation rates, and decay parameters for mRNAs of thousands of individual genes, which in turn provided fundamental insights into cytoplasmic mRNA metabolism.

RESULTS

Global Profiling of Tail-Length Dynamics

Two high-throughput methods, each with distinct advantages, were initially developed to profile poly(A)-tail lengths. One is PAL-seq (poly(A)-tail-length profiling by sequencing), which also reports the cleavage-and-polyadenylation site for each polyadenylated molecule (Subtelny et al., 2014), whereas the other is TAIL-seq, which can measure poly(A) tails that have been terminally modified with non-A residues (Chang et al., 2014; Lim et al., 2016). Here, we developed PAL-seq version 2 (v2), which combines these advantages and has the further benefit over both previous methods of more robust compatibility with contemporary Illumina sequencing platforms (Figure S1).

To observe tail-length dynamics of endogenous mRNAs, we employed a metabolic-labeling approach in which mRNAs of different age ranges were isolated and analyzed (Figure 1A). To initiate labeling, we added 5-ethynyl uridine (5EU) to 3T3 cells.

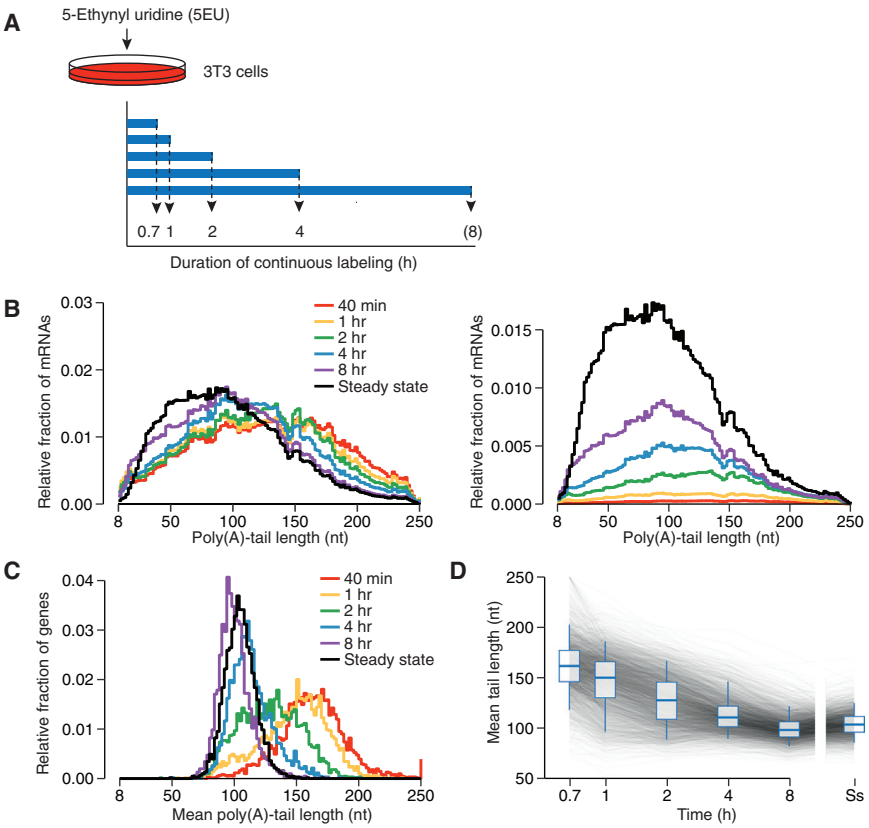

Figure 1. Global Tail-Length Dynamics of Mammalian mRNAs

(A) Schematic of 5EU metabolic labeling. Experiments were performed with two 3T3 cell lines designed to induce expression of either miR-155 or miR-1 (cell lines 1 and 2, respectively) but cultured without microRNA induction. The 8 is in parentheses because an 8-h labeling period was included for only one line (cell line 1). For simplicity, all subsequent figures show the results for cell line 1, unless stated otherwise.

(B) Tail-length distributions of mRNA molecules isolated after each period of 5EU labeling (key). Left: distributions were normalized to each have the same area. Right: distributions were scaled to the abundance of labeled RNAs in each sample and then normalized such that the steady-state sample had an area of 1. The steady-state sample was prepared with unselected RNA from the 40-min time interval. Each bin is 2 nt; results for the bin with tail lengths $\geq$ 250 nt are not shown.

(C) Distributions of mean poly(A)-tail lengths for mRNAs of each gene after the indicated duration of 5EU labeling. Values for all genes that passed the tag cutoffs for tail-length measurement at all time intervals were included (n = 3,048). Each bin is 2 nt. Genes with mean mRNA tail-length values greater than $\geq$ 250 nt were assigned to the 250-nt bin.

(D) Tail lengths over time. Mean tail lengths for mRNAs from each gene (n = 3,048) are plotted along with box-and-whiskers overlays (line, median; box, 25th–75th percentiles; whiskers, 5th–95th percentiles). Ss, steady state. See also Figures S1 and S2.

After incubating for time periods ranging from 40 min to 8 h, cytoplasmically enriched lysates were collected, and RNA containing 5EU was isolated by virtue of the reactivity between the 5EU and an azide-bearing biotin tag. Poly(A)-tail lengths of captured mRNAs, as well as total-lysate mRNA, were measured using PAL-seq v2 (hereafter called PAL-seq). In parallel, we performed RNA-seq, which measured mRNA abundance for each time interval. Spike-in of RNA standards with known tail lengths enabled estimates of recovery and measurement accuracy over a broad range of tail lengths, as well as absolute quantification of RNA measured by each method. These experiments were performed using each of two independently passaged 3T3 cell lines. Unless stated otherwise, figures show the results obtained for cell line 1. Nonetheless, the results of the two cell lines were reproducible at each time interval ($R_s \geq 0.81$ for mean tail-length measurements). Moreover, results from either PAL-seq v1, PAL-seq v2, or our implementation of TAIL-seq were highly correlated (Figures S2A–S2D; R_s = 0.83–0.88 for each of the two-way comparisons), which indicated that our conclusions were independent of the method used for tail-length profiling.

As expected if tail lengths become shorter over time in the cytoplasm (Sheiness and Darnell, 1973; Palatnik et al., 1979), mRNAs collected after the shortest labeling period (40 min) had the longest poly(A)-tail lengths, with median length of 133 nt (Figure 1B). As the average age of each labeled mRNA population increased with longer labeling periods, tail-length distributions shifted toward the steady-state distribution with respect to both length and abundance (Figure 1B). At each time interval, 10–20-nt tails preferentially possessed a 3′ terminal U (Figure S2E), although < 6.8% of tails had 3′ U residues in any sample, in keeping with previous reports on the fraction of short tails with terminal uridines at steady state (Chang et al., 2014; Lim et al., 2014). Analyses of mean poly(A)-tail lengths for mRNAs corresponding to thousands of individual genes showed that tails from mRNAs of essentially every gene shortened over time in the cytoplasm (Figures 1C and 1D).

Correspondence between mRNA Half-Life and Deadenylation Rate

After 2 h of labeling, a broad range of mean tail lengths was observed, as mean tail lengths for mRNAs of some genes approached their steady-state values, whereas those for others still resembled their initial values (Figure 1C). These different rates of approach to steady state presumably at least partly reflected differences in mRNA degradation rates, as short-lived mRNAs were expected to reach their steady-state abundance and poly(A)-tail length more rapidly than long-lived mRNAs.

To determine these degradation rates, we fit the yield of PAL-seq tags obtained for each gene at each time interval (normalizing to the spike-in controls) to the exponential function describing the approach to steady state, while also fitting a global offset to account for a delay between the time that 5EU was added and the time that labeled mRNAs appeared in the cytoplasm. This offset ranged from 27 to 36 min, depending on the experiment, a range

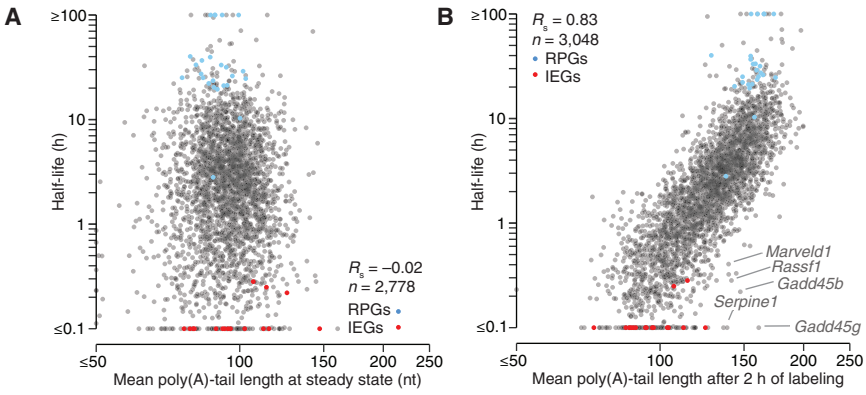

Figure 2. Correspondence between mRNA Half-Life and Deadenylation Rate

(A) Relationship between half-life and mean steady-state tail length of mRNAs in 3T3 cells. For mRNAs of each gene, standard PAL-seq data were used to determine the length distribution of tails ≥ 50 nt, and data generated from a protocol that used single-stranded ligation to the mRNA 3′ termini (rather than a splinted ligation to the tail) were used to determine both the length distribution of tails < 50 nt and the fraction of tails < 50 nt. Compared to the tail-length distribution generated by only standard PAL-seq data, this composite distribution better accounted for very short and highly modified tails. Nonetheless, using the standard PAL-seq data without this adjustment produced a similar result (Figure S3G). Results for mRNAs of ribosomal protein genes (RPGs) and immediate-early genes (IEGs) (Tullai et al., 2007) are indicated (blue and red, respectively).

(B) Relationship between mRNA half-life and mean tail length of metabolically labeled mRNAs isolated after 2 h of labeling. Otherwise as in (A).

See also Figures S3A–S3D and S3G.

consistent with single-gene measurements of the time required for mRNA transcription, processing, and export (Shav-Tal et al., 2004; Mor et al., 2010). Our half-life values (Table S1) correlated well with those previously reported for mRNAs of 3T3 cells growing in similar conditions (Schwanhäusser et al., 2011) (Figure S3A; R_s = 0.68–0.77), although our absolute values were substantially shorter (Figures S3B–S3D; median 2.1 h for mRNAs of the 3T3 cell line 1, as opposed to 9 h for previously reported values). This difference was attributable to potential divergence in the cell lines used in the two labs, as well as our focus on cytoplasmically enriched RNA and our absolute quantification of labeled RNA (enabled by spiking in standards).

Previous global analyses of the relationship between mRNA half-life and mean tail length have been limited to steady-state tail-length measurements, for which no positive relationship is observed (Subtelny et al., 2014), despite the established role of poly(A) tails in conferring mRNA stability. Our current datasets, which provided the opportunity to make this comparison using half-life and tail-length measurements acquired from the same cells, reinforced this finding; we observed no positive relationship between mRNA half-life and mean steady-state tail length (Figure S3G; R_s = −0.24). This result held when incorporating results of PAL-seq implemented with direct ligation to mRNA 3′ termini, which better detected very short or highly modified tails (Figure 2A; R_s = −0.02). Indeed, the mean tail lengths of long-lived mRNAs, including those of ribosomal protein genes (RPGs), closely resembled tail lengths of short-lived mRNAs, including those of immediate-early genes (IEGs) (Figure 2A).

A very different picture emerged when considering pre-steady-state tail-length measurements. After 2 h of labeling, half-life strongly corresponded to mean tail length (Figure 2B; R_s = 0.83). At this labeling interval, IEG mRNAs and other short-lived mRNAs had the shortest mean tail lengths, RPG mRNAs and other long-lived mRNAs had the longest mean tail lengths, and other mRNAs had mean tail lengths falling somewhere in between. The simplest explanation for this result is that the deadenylation rate dictates the stability of most mRNAs, and mean tail length at 2 h provides a proxy for deadenylation rate. Thus, slow deadenylation of long-lived mRNAs explains both why they have longer tails after 2 h of labeling and why they have such long half-lives, and rapid deadenylation of short-lived mRNAs explains why they have shorter tails after 2 h of labeling and why they have such short half-lives.

Several notable outliers had half-lives that were shorter than expected from their mean tail lengths in the 2-h sample, suggesting that their degradation and deadenylation rates were incongruous. *Rassf1*, *Serpine1*, and two *Gadd45* paralogs are known or suspected substrates for either nonsense-mediated decay (NMD) or other pathways that recruit UPF1 (Nelson et al., 2016; Park and Maquat, 2013; Tani et al., 2012). Another outlier, the *Marveld1* mRNA, has not yet been reported to interact with UPF1, but its protein product does interact with UPF1 in human cells and regulates UPF1 activity (Hu et al., 2013). Association with UPF1 can trigger endonucleolytic cleavage of mammalian mRNAs, which would decouple the rates of decay and deadenylation (Mühlemann and Lykke-Andersen, 2010), disrupting the relationship between half-life and tail length at intermediate labeling intervals. Nonetheless, the most notable feature of the outliers was their scarcity; the striking overall correspondence observed between half-life and mean tail lengths after 2 h of labeling implied that for the vast majority of endogenous mRNA molecules of mouse fibroblasts, the rate of mRNA deadenylation largely determines the rate of degradation.

Initial Tail Lengths of Cytoplasmic mRNAs

Analysis of tail-length distributions for individual genes and the changes in these distributions over increased labeling intervals supported and extended the conclusions drawn from global analyses of abundances and mean tail lengths. This analysis confirmed that tail-length dynamics of mRNAs with short half-lives (e.g., *Metrnl*) substantially differed from those of mRNAs with longer half-lives (e.g., *Lsm1* and *Eef2*), with the short-lived mRNAs reaching their steady-state abundance and tail-length distribution much more rapidly (Figure 3). The stacked pattern of the distributions observed over increasing time intervals also illustrated that the longest-tailed mRNAs observed at steady state were essentially all recently transcribed, whereas the shortest-tailed mRNAs were mostly the oldest mRNAs (Figure 3).

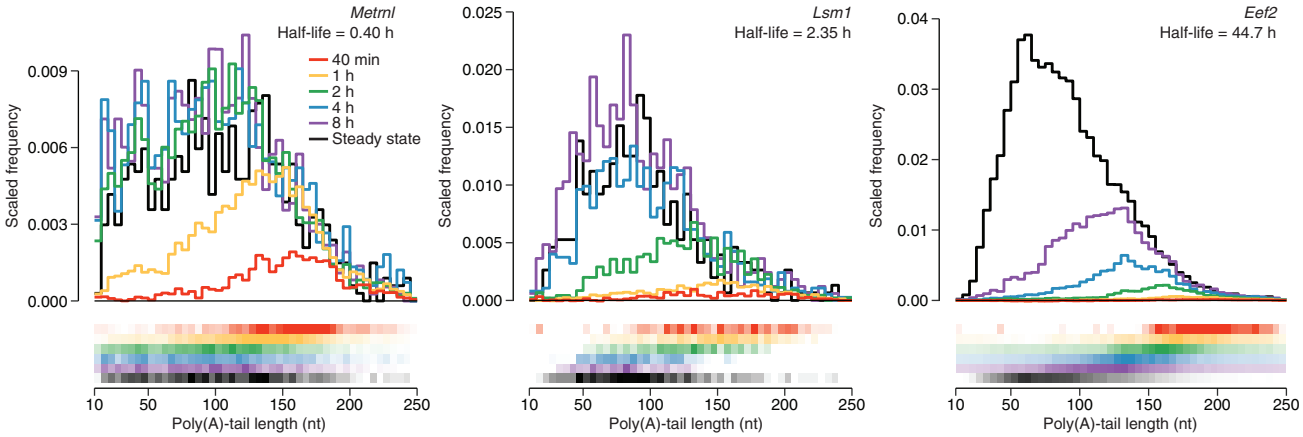

Figure 3. Tail-Length Dynamics of mRNAs with Different Half-Lives

Tail-length distributions for mRNAs from individual genes. For each time interval (key), the distribution is scaled to the abundance of labeled RNA in the sample (top), and the distribution is also represented as a heatmap (bottom), with the range of coloration corresponding to the 5th–95th percentiles of the histogram density. Each bin is 5 nt. Bins for tails < 10 nt are not shown because the splinted ligation to the tail used in the standard PAL-seq protocol depletes measurements for tails < 8 nt. Bins for tails ≥ 250 nt are also not shown.

See also Figures S3F and S3H–S3J.

Our tail-length data from short labeling periods provided the opportunity to examine the initial tail lengths of mRNAs soon after they entered the cytoplasm. The calculated 27–36-min delay in the appearance of labeled cytoplasmic mRNAs implied that most mRNAs isolated after 40 min of labeling were subject to cytoplasmic deadenylation for < 13 min. Thus, for all but the most rapidly deadenylated mRNAs, the tail lengths observed after 40 min of labeling should have approximated the tail lengths of mRNAs that first entered the cytoplasm.

Without data to the contrary, previous studies of tail-length dynamics have assumed that initial cytoplasmic tail lengths observed for mRNAs of one gene also apply to the mRNAs of all other genes. However, we observed substantial intergenic variation for average tail lengths at the shortest labeling period (Figures 1C, 3, and S3F), with the spread of the 5th–95th percentile values at least that of steady state (112.2 ± 4.7 to 194.7 ± 6.0 nt for the 40-min samples and 84.8 ± 1.3 to 124.6 ± 2.1 nt for the steady-state samples; values ± SD), which suggested that mRNAs from different genes exit the nucleus with tails of quite different lengths. To examine whether deadenylation occurring soon after nucleocytoplasmic export might have influenced this result, we focused on mRNAs with half-lives > 8 h. On average, mean tail lengths for these genes exhibited less than 4% change when comparing the 40-min and 1-h time intervals, implying that they also underwent little cytoplasmic deadenylation during the first 40 min of labeling. Average tail lengths observed at 40 min for mRNAs from these genes spanned a broad range, exceeding that observed at steady state (spread of the 5th–95th percentile values 128.3 ± 5.2 to 242.1 ± 16.1 nt for the 40-min samples and 81.0 ± 1.0 to 119.4 ± 1.4 nt for the steady-state samples; values ± SD), although these tail-length values observed at 40 min had little correspondence with those observed at steady state (R_s = 0.12).

When comparing mRNAs from the same gene, tail-length distributions were also quite broad for the newly exported mRNAs, as illustrated for mRNAs from three genes (Figure 3), and further demonstrated by the mean coefficient of variation (c.v.) of 0.41 for mRNAs of all measured genes (Figure S3H), compared to a c.v. of 0.20 for the 160-nt standard spiked into the 40-min sample. These c.v. values were reproducible between biological replicates and had little correspondence with mRNA half-life (Figures S3I and S3J). Although we cannot rule out the formal possibility that mRNA tails undergo exceedingly rapid and variable transient deadenylation immediately upon nuclear export, we interpret our results at short labeling periods to indicate that mRNAs exit the nucleus with considerable but reproducible intergenic and intragenic tail-length variability.

A Quantitative Model of mRNA Deadenylation and Decay

Our ability to isolate mRNAs of different age ranges for each gene and analyze their abundances and tail lengths (Figure 3) provided the unique opportunity to calculate the deadenylation rates and other metabolic rates and parameters for these mRNAs, thereby expanding the number of metabolically characterized mammalian mRNAs far beyond the four (*Mt1*, *Fos*, *Hbb*, and *IL8*) that have been examined using single-gene measurements (Mercer and Wake, 1985; Wilson and Treisman, 1988; Shyu et al., 1991; Gowrishankar et al., 2005). For each gene, the number of mRNA molecules with a given tail length is a function of (1) the rate of mRNA entering the cytoplasm, which in turn is a function of the rates of transcription, processing, and nucleocytoplasmic export; (2) the tail-length distribution of mRNA entering the cytoplasm; (3) the deadenylation rate; (4) the tail length below which the mRNA body is no longer protected from decay; and (5) the decay rate of the mRNA body (presumably preceded by decapping). Therefore, we developed a mathematical model to determine, for mRNAs from thousands of genes, values for each of these parameters.

Our model was based on a system of differential equations that describe the rates of change of abundance of mRNA intermediates (Figure 4A; Table S2), an approach resembling that

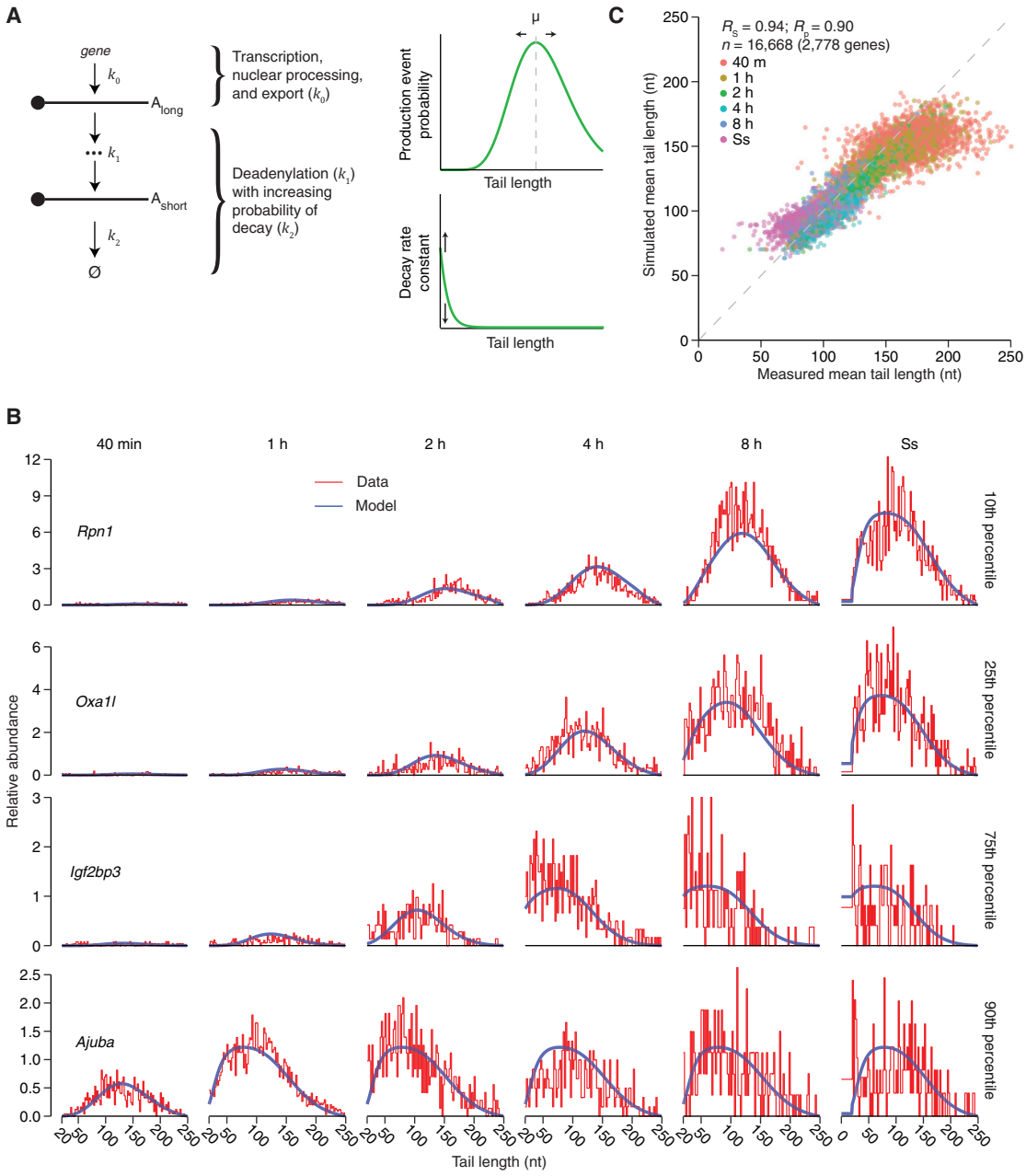

Figure 4. Computational Model of mRNA Deadenylation and Decay Dynamics

(A) Schematic of the computational model. k_0, k_1, and k_2 are terms for mRNA production, deadenylation, and decay, respectively, and ∅ represents the loss of the mRNA molecule. The curves (right) indicate the distributions used to model probabilities of production and decay as functions of tail length. They are schematized using the globally fitted parameters (v_p, m_d, and v_d) that defined each distribution (Table S2). The parameter m_p controls the mean (μ) of the negative binomial distribution (top curve), whereas the decay rate constant, β, scales the decay distribution (bottom curve) (Table S2).

(B) Correspondence between the model and the experimental data. Results for mRNAs of these four genes are shown as representative examples because their fits fell closest to the 10th, 25th, 75th, and 90th percentiles of the distribution of R^2 values for all genes that passed expression cutoffs in the PAL-seq datasets (Figure S4F; n = 2,778). For each time interval, the blue line shows the fit to the model, and the red line shows the distribution of observed tail-length species, plotted in 2-nt bins and scaled to standards as in Figure 1B, right. Ss, steady state.

(C) Correspondence between mean tail lengths generated from the model simulation and tail lengths measured in the metabolic labeling experiment. Shown for each gene are mean tail lengths for mRNAs at each time interval (key) from the simulation plotted with respect to the values observed experimentally. The discrepancy observed for some mRNAs at early time intervals was attributable to low signal for long-lived mRNAs at early times. The dashed line indicates $y = x$. See also Figures S4, S5A, and S5B and Tables S1 and S2.

used to model the metabolism of RNAs from single-gene reporters (Cao and Parker, 2001; Jia et al., 2011). For each gene, transcription, nuclear processing, and export (hereafter abbreviated as "production") generates, with rate constant k_0, a distribution of initial poly(A)-tail lengths. Over time, deadenylation shortens the tail, one nucleotide at a time, with rate constant k_1. Decay of the mRNA body, with rate constant k_2, can occur alongside deadenylation and monotonically increases as the poly(A) tails get shorter. One interpretation of this deadenylation-dependent decay is that it represents decapping, followed by rapid degradation of the mRNA body. However, because we do not monitor cap status, our model was not designed to distinguish between decay mechanisms and is compatible with either 5′ or 3′ exonucleolytic decay of the mRNA body.

For individual mRNAs generated from the same gene, the production terms varied according to a negative binomial distribution—a distribution routinely used to model the probability of a failure after a series of successes (in our case, creating an mRNA of tail length $n + 1$ after successfully creating an mRNA of tail length n) (Figure 4A; Table S2). The decay rate constant (k_2) followed a logistic function, which accelerated as tails shortened. The two parameters of this function (m_d and v_d) were fit as global constants, while the scaling parameter (β) was fit to each gene (Table S2). Solving the differential equations of the model estimated both the tail-length distribution and the mRNA abundance at each time interval for mRNAs from each gene.

Before arriving at the final version of the model (Figure 4A), we considered alternative models with varying levels of complexity. For example, building on the proposal that most mRNAs are substrates for both the PAN2/PAN3 and CCR4/NOT deadenylase complexes, with PAN2/PAN3 acting on tails > 110 nt and CCR4/NOT acting on shorter tails (Yamashita et al., 2005), we tested the performance of a model with two deadenylation rate constants, in which the transition between the two occurred at a tail length of 110 nt (Figure S4A). This model yielded residuals that were only marginally improved (Figure S4B), and for each mRNA the two deadenylation rates resembled each other (Figure S4C). A model in which the transition between the deadenylation rates occurred at 150 nt (Yi et al., 2018) yielded similar results (Figures S4D and S4E). These results indicated that, for endogenous mRNAs in 3T3 cells, either a single deadenylase complex dominates—as recently proposed for mRNAs with tail lengths $\leq$ 150 (Yi et al., 2018)—or both complexes act with indistinguishable kinetics. Thus, we chose not to implement a more complex model with two deadenylation rate constants.

Fitting the final version of the model to the tail-length and abundance measurements for mRNAs from thousands of genes yielded average initial tail lengths and rate constants for production, deadenylation, and deadenylation-dependent decay for each of these mRNAs (Table S2). The correspondence between the output of the model and the experimental measurements is illustrated for genes selected to represent different quantiles of fit based on the distribution of R^2 values (Figure 4B; Figure S4F). Mean tail-length values generated by the model corresponded well to measured values (Figure 4C; $R_s = 0.94$, $R_p = 0.90$). Moreover, values fit for starting tail length, production, deadenylation, and deadenylation-dependent decay were reproducible between biological replicates and robust to parameter initialization as well as multinomial sampling (bootstrap analysis) (Figures S4G–S4J).

The Dynamics of Cytoplasmic mRNA Metabolism

Of the six yeast mRNAs and four mammalian mRNAs that have been metabolically characterized, the data for four yeast mRNAs and two mammalian mRNAs are of sufficient resolution to derive deadenylation rates. The two mammalian mRNAs, *Fos* and *Mt1*, have deadenylation rate constants that differ by 60-fold (20 and 0.33 nt/min, respectively) (Mercer and Wake, 1985; Shyu et al., 1991). Our analysis, which characterized the metabolism of 2,778 mRNAs, greatly expanded the set of mRNAs with measured deadenylation rates and showed that deadenylation rate constants of mammalian mRNAs can differ by > 1000-fold—as fast as > 30 nt/min and as slow as 1.8 nt/h (Figure 5A). Concordant with our direct analysis of the primary data, which indicated that most mRNAs degrade through a mechanism involving tail shortening (Figure 1F), mRNA half-lives corresponded strongly to deadenylation rate constants fit to our model ($R_s = -0.95$; Figure S5A).

Our model and its fitted parameters allowed us to compute the deadenylation-dependent decay rates at each tail length and thereby infer the tail lengths at which mRNAs were degraded (Figure 5B). This analysis indicated that nearly all decay of the mRNA body occurred after the tail lengths fell below 100 nt, which agreed with previous analyses of reporter genes (Yamashita et al., 2005). Decay accelerated as tail lengths fell below 50 nt (with > 92% of mRNAs decaying below this length), a length less than the 54-nt footprint of two adjacent cytoplasmic poly(A)-binding protein (PABPC) molecules (Baer and Kornberg, 1983; Yi et al., 2018), but most mRNA molecules (> 55%) did not decay until their tail lengths fell below 25 nt, a length less than the 27-nt footprint of a single PABPC molecule (Figure 5B).

When analyzing for mRNAs of each gene the mean tail length at which the mRNA body decays, the results generally concurred with those observed for all mRNAs combined, with mRNAs from most genes decaying at short mean tail lengths (Figure 5C; > 97% decaying at mean tail length < 50 nt and > 69% decaying at mean tail length < 25 nt). As expected, most mRNAs previously found to have discordant deadenylation and decay rates (Figure 1F) were also outliers in this analysis, with *Gadd45b* and *Marveld1* degrading at mean tail lengths of 62, and 59 nt, respectively. The estimates of mean tail lengths at which mRNAs decay together with initial tail lengths and deadenylation rate constants enabled estimates of the time required to reach the mean tail length of decay, which corresponded to lifetime slightly better than did the deadenylation rate constants on their own to half-life (Figures S5A and S5B; $R_s = -0.96$ and -0.95, respectively.)

Once tails reached a short length, the decay rate constants varied widely, with short-tailed mRNAs from some genes undergoing decay at rate constants > 1000-fold greater than those of short-tailed mRNAs from other genes (Figure 5D). *Fos*, a rapidly deadenylated mRNA, is degraded much faster upon reaching a short tail length than is *Hbb*, a less rapidly deadenylated mRNA (Shyu et al., 1991). More rapid degradation of short-tailed mRNAs that had been more rapidly deadenylated would help prevent the buildup of short-tailed isoforms of rapidly

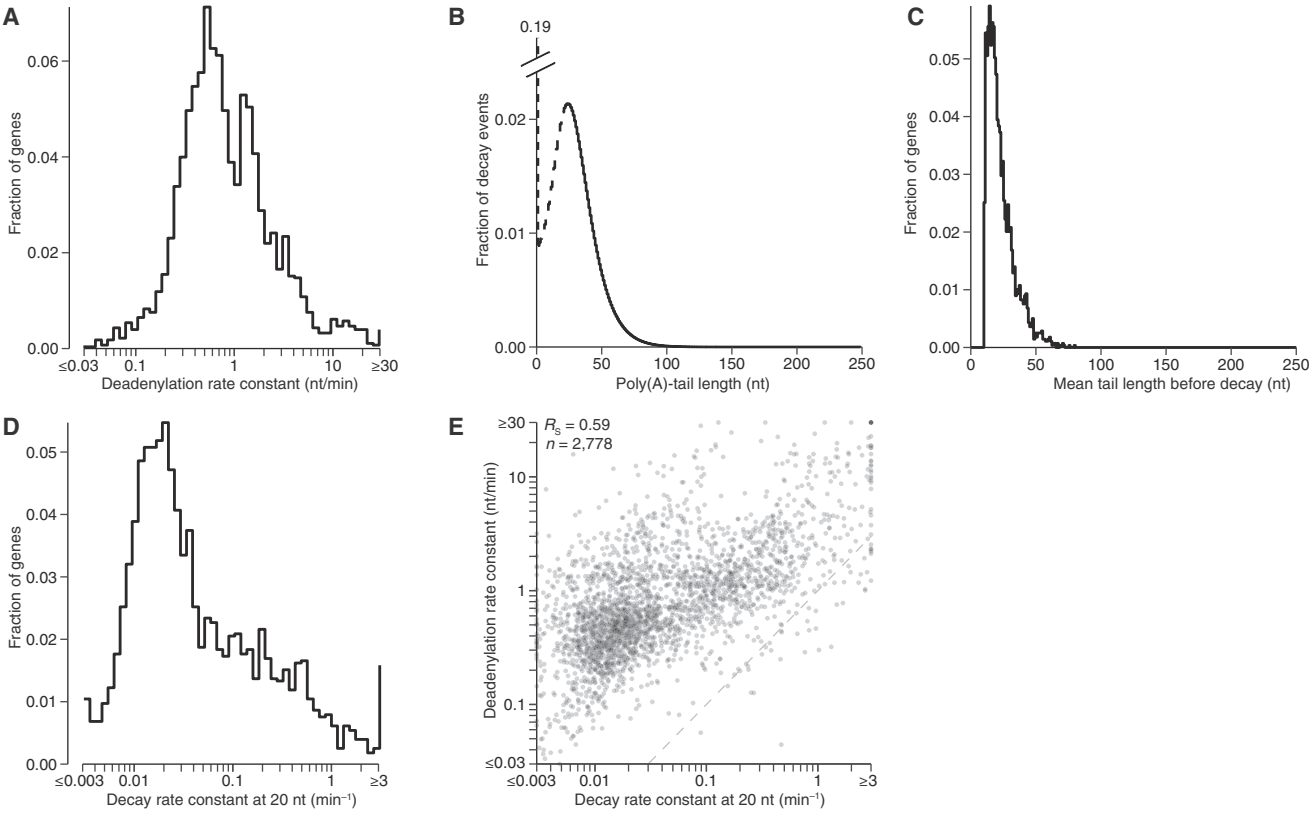

Figure 5. Dynamics of Cytoplasmic mRNA Metabolism

(A) Distribution of deadenylation rate constants (k_1 values), as determined by fitting the model to data for mRNAs from each gene (n = 2,778).

(B) Tail lengths at which mRNAs decay, as inferred by the model. The model rate constants were used to simulate a steady-state tail-length distribution for each gene. The abundance of each mRNA intermediate was then multiplied by the decay rate constant k_2 to yield a distribution of decay events over all tail lengths. Plotted is the combined distribution for all mRNA molecules of all 2,778 genes. Results were indistinguishable when the distribution from each gene was weighted equally. Values for tails < 20 nt are shown as a dashed line because the model fit steady-state tail lengths < 20 nt as an average of the total abundance of tails in this region and, thus, did not provide single-nucleotide resolution for decay rates of these species.

(C) Mean tail lengths at which mRNAs from each gene (n = 2,778) decayed, as inferred by the model. Otherwise, as in (B).

(D) Distribution of decay rate constants (k_2 values) for mRNAs with 20-nt tail lengths, as determined by fitting the model to data for mRNAs from each gene (n = 2,778).

(E) Correlation between the deadenylation rate constant (k_1) and the decay rate constant (k_2) at a tail length of 20 nt. The dashed line indicates $y = x$.

See also Figure S4.

deadenylated mRNAs. However, such buildup sometimes does occur, as observed in *Drosophila* cells for three mRNAs characterized during heat shock (Dellavalle et al., 1994; Bönisch et al., 2007) and in mammalian cells for *Csf2* (Chen et al., 1995; Carballo et al., 2000), raising the question of the extent to which decay rates of short-tailed mRNAs are coupled to their deadenylation rates. To answer this question, we examined the relationship between rate constants for deadenylation and those for decay of short-tailed mRNAs (the latter calculated for mRNAs with 20-nt tails). We found that more rapidly deadenylated mRNAs tended to be degraded more rapidly upon reaching short tail lengths (Figure 5E; R_s = 0.59).

A Modest Buildup of Short-Tailed Isoforms of Short-Lived mRNAs

Having found a strong tendency for more rapid clearing of mRNAs that had been more rapidly deadenylated, we investigated whether this phenomenon was able to prevent a large buildup of short-tailed isoforms of rapidly deadenylated mRNAs. For this investigation, we analyzed the steady-state dataset that incorporated results of PAL-seq implemented with direct ligation to mRNA 3′ termini, which better detected very short or highly modified tails. Despite the rapid decay of short-tailed mRNAs that had been more rapidly deadenylated, less-stable mRNAs generally did have a somewhat higher fraction of short-tailed transcripts (Figures 6A and S5C; R_s = −0.56). Nonetheless, the buildup of short-tailed isoforms of these unstable RNAs usually failed to exceed 30% of all transcripts (Figure 6A).

This preferential buildup of short-tailed isoforms of unstable RNAs was more clearly visualized in a meta-transcript analysis of the tail-length distribution at steady state. Short-lived mRNAs (half-lives < 20 min) had two peaks of short-tailed isoforms, a major peak centering at 7–15 nt and a minor peak at 0–1 nt, whereas long-lived mRNAs (half-lives > 10 h) were depleted of

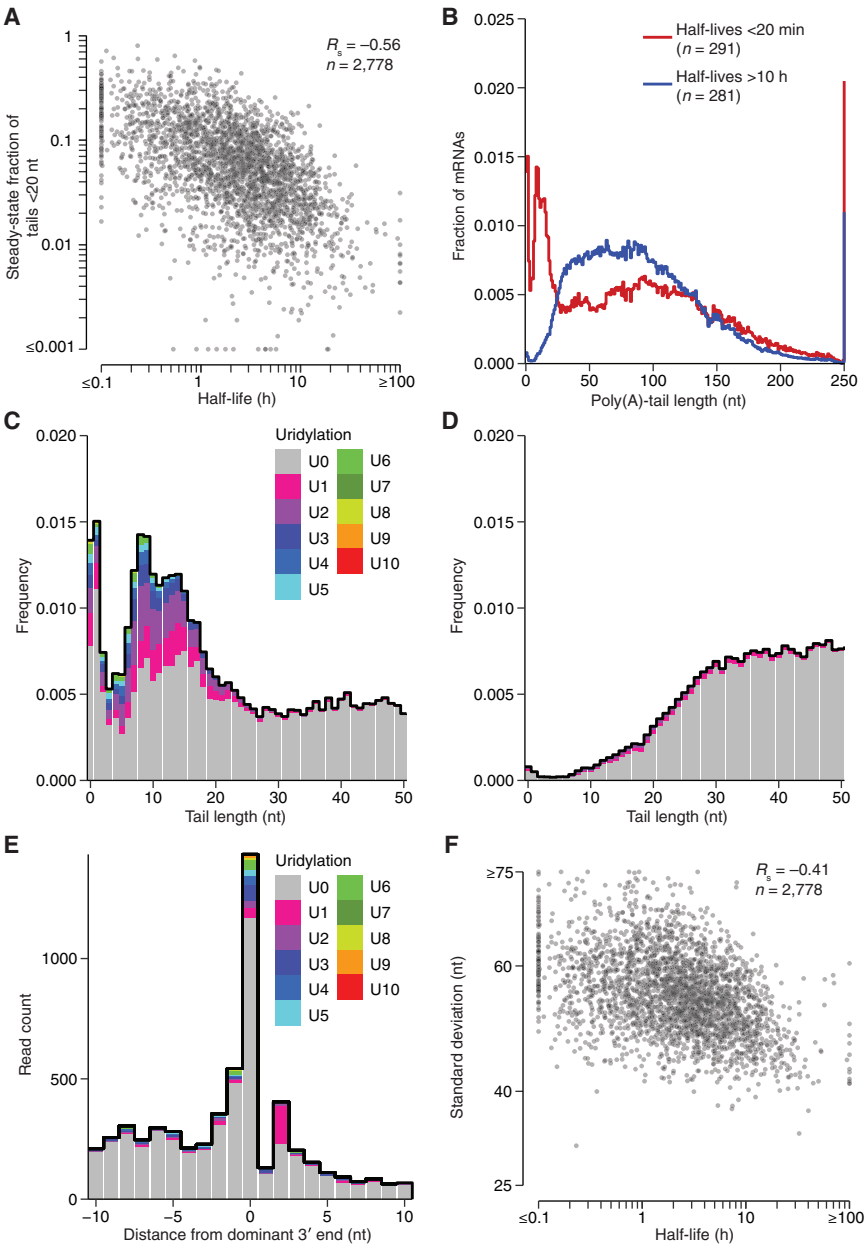

Figure 6. A Modest Buildup of Short-Tailed Isoforms of Short-Lived mRNAs

(A) Relationship between the steady-state fraction of tails < 20 nt and mRNA half-life. For mRNAs of each gene, the fraction of tails < 20 nt was calculated from a composite distribution generated as in Figure 2A, which accounted for very short and highly modified tails.

(B) Metatranscript distributions of steady-state tail lengths of short- and long-lived mRNAs (red and blue, respectively), with mRNAs from each gene contributing density according to their abundance. Results were almost identical when mRNAs were weighted such that each gene contributed equally. This analysis used the composite distributions as in (A).

(C) Uridylation of short-lived mRNAs with short poly(A) tails. For mRNAs with half-lives < 20 min, the fraction of molecules with the indicated poly(A)-tail length at steady state is plotted, indicating for each tail length the proportion of tails appended with 0 through 10 U nucleotides (key). For mRNAs with poly(A)-tail length of 0, U residues were counted only if they could not have been genomically encoded. As poly(A) tails approached 20 nt, the ability to map reads with ≥ 3 terminal U residues diminished, but the ability to map reads with 1–2 terminal U residues was retained for poly(A) tails of each length.

(D) Uridylation of long-lived mRNAs (half-lives > 10 h) with short poly(A) tails. Otherwise as in (C).

(E) Distribution of tailless tags (regardless of mRNA half-life) as a function of their distance from the annotated 3′ end of the UTR. Tags with a terminal A (or with a terminal A followed by one or more untemplated U) were excluded, even if the A might have been genomically encoded. The proportion of tails appended with 0 through 10 U nucleotides is shown (key).

(F) Relationship between the standard deviation of steady-state tail length and mRNA half-life. Otherwise as in (A).

See also Figures S5C–S5J.

tails of < 20 nt (Figure 6B). Closer inspection of these two peaks revealed that these short-tailed isoforms of short-lived mRNAs were dramatically enriched in mono- and oligouridylated termini (Figures 6C, 6D, and S5D), consistent with studies showing that uridylation occurs preferentially on shorter tails and helps to destabilize mRNAs (Kwak and Wickens, 2007; Rissland et al., 2007; Rissland and Norbury, 2009; Chang et al., 2014; Lim et al., 2014), and further indicating that uridylation occurs preferentially on short-lived mRNAs.

The observation of a 0–1-nt peak in the steady-state tail-length distribution prompted examination of fully deadenylated isoforms of mRNAs that were initially polyadenylated. Molecules without tails were often also missing the last few nucleotides of the 3′ UTR (Figures 6E and S5E), suggesting that after removing the tail, the deadenylation machinery (or some other 3′-to-5′ exonuclease) usually proceeds several nucleotides into the mRNA body. Analysis of mRNAs with tails indicated that, with few exceptions, the last nucleotide of the 3′ UTR was consistently defined (Figures S5F–S5H), which supported the idea that the missing nucleotides of tailless molecules had not been lost during the process of cleavage and polyadenylation. Analysis of the final dinucleotides of tailless tags revealed no consistent pattern after accounting for the genomic background, suggesting that other factors, such as proteins or more distal nucleotide composition, influence the position at which the exonuclease stops.

Despite their presence, the two peaks of short-tailed isoforms did not dominate the distribution, as most short-lived mRNAs (70%) had tails exceeding 30 nt (Figure 6B). Indeed, compared to long-lived mRNAs, these short-lived mRNAs also had modest enrichment for very long tails (> 175 nt) (Figures 6B, S5I, and S5J), perhaps due to an initial lag in assembling deadenylation machinery as mRNAs enter the cytoplasm, which would cause a relatively larger fraction of short-lived mRNAs to exist in the cytoplasm prior to an initial encounter with a deadenylase. The increased fractions of both short-tail and long-tail isoforms for short-lived mRNAs led to broader overall tail-length distributions (Figure 6B) with increased standard deviations in tail length (Figure 6F; $R_s = -0.41$). Moreover, the increased fractions of shorter and longer isoforms offset each other when calculating mean tail length, leading to similar mean tail lengths for the short- and long-lived mRNAs (Figure S5K; median mean tail lengths = 89 and 92 nt, respectively), which contributed to the lack of correlation between half-life and mean tail length at steady state (Figure 2A). Most importantly, the low magnitude of the buildup supported our conclusion that for most mRNAs the steps of deadenylation and subsequent decay are kinetically coupled: short-tailed mRNAs that had previously undergone more rapid deadenylation are more rapidly degraded. This coupling prevents a large buildup of short-tailed isoforms of rapidly deadenylated RNAs, thereby enabling the large range in deadenylation rate constants to impart a similarly large range in mRNA stabilities.

Deadenylation and Decay Dynamics of Synchronous mRNA Populations

Our continuous-labeling experiments were designed to measure the dynamics of mRNA metabolism in an unperturbed cellular environment. However, this framework required deadenylation and deadenylation-dependent decay parameters to be inferred as mRNAs from each gene approached their steady-state expression levels and tail lengths, with their populations becoming progressively less synchronous, causing the signal for their end behavior to be diluted. For orthogonal measurements of these parameters, we performed a pulse-chase-like experiment that more closely resembled previous studies with single-gene reporters, in that it monitored synchronous populations of mRNAs from each gene. After a 1-h pulse of 5EU, 3T3 cells were treated with actinomycin D (actD) to block transcription, and abundances and poly(A)-tail lengths of the mRNAs produced during the 5EU-labeling period were measured over the next 15 h, thereby revealing the behavior of synchronized mRNA populations as they age (Figure 7A).

As expected, tail lengths of labeled mRNAs progressively decreased after transcriptional inhibition, with median lengths shortening from 123 to 51 nt over the course of the experiment (Figure 7B). Examination of mean tail lengths of mRNAs from each gene revealed a similar trend (Figure 7C). At later time points mean tail-length distributions peaked between 45 and 50 nt (Figure 7C), far below the 100–105-nt mode of the steady-state distribution, which included mRNAs of all ages (Figure 1C).

The actD treatment had some side effects. At later time points, a ~30-nt periodicity emerged in the single-molecule tail-length distributions (Figure 7B). Although such phasing of tail lengths, with a period resembling the size of a PABPC footprint, has been observed in mammalian cells following CCR4 knockdown (Yi et al., 2018) and in *C. elegans* (Lima et al., 2017), only subtle phasing was observed in unperturbed mammalian cells (Figure 6B). The more prominent periodicity observed after prolonged actD treatment was presumably the result of more dense packing of PABPC on poly(A) tails in the context of a diminishing mRNA pool. A second side effect of actD treatment concerned mRNA half-lives, which increased from a median of 2.1 h in the continuous-labeling experiment to a median of 3.8 h in the transcriptional-shutoff experiment (Figure S3E). This increase was observed even for mRNAs with the shortest half-lives, which indicated that it occurred before actD could have influenced protein output, i.e., in less time than that required for mRNA nucleocytoplasmic export and translation. This result generalized previous observations concerning the effects of actD on reporter-mRNA stabilities (Chen et al., 1995).

Despite the side effects of actD, the rank order of mRNA half-lives determined from the transcriptional-shutoff experiment agreed well with that from the continuous-labeling experiment (Figure S3E; $R_s = 0.78$), indicating that the transcriptional-shutoff experiment captured key aspects of the unperturbed condition. In addition, mRNA half-lives calculated from the continuous-labeling experiment strongly corresponded to mean tail length observed 1 h after actD treatment (Figure 7D; note that 1 h after actD treatment was 2 h after 5EU labeling and thus most comparable to Figure 2B). Indeed, the strength of the correspondence between half-life and 1-h tail length ($R_s = 0.88$) further supported our conclusion that the vast majority of mRNAs are primarily degraded through deadenylation-linked mechanisms.

To further analyze the results of the transcriptional-shutoff experiment, we grouped mRNAs into cohorts based on their half-lives and monitored the abundance and average tail length of mRNAs from individual genes at each time point (Figure 7E). Regardless of mRNA half-life, tails initially shortened with little change in abundance until mean tail lengths fell below 100 nt. As expected based on the strong correspondence between half-life and 1-h tail length (Figure 7D), mRNAs with shorter half-lives underwent more rapid tail shortening (Figure 7E). Once mean tail lengths fell below 50 nt (implying that a substantial fraction of tails fell below 25 nt), degradation accelerated. This acceleration was more prominent for mRNAs with shorter half-lives, which confirmed our conclusion that short-tailed mRNAs that had undergone more rapid deadenylation are also more rapidly degraded (Figure 7E).

To examine how well our model predicted this behavior, we used it to predict the results of the transcriptional-shutoff experiment, using the rate constants measured earlier from the continuous-labeling experiment. When simulating a shorter time course to account for the more rapid deadenylation and decay observed without actD, the results predicted by the model agreed well with the experimental observations ($R_s = 0.93$ and 0.61 for mean tail length and abundance, respectively; $n = 11{,}273$ values above the abundance threshold for 2,687 mRNAs), including the precipitous decline in abundance when mean tail lengths fell below 50 nt and the faster degradation of short-tailed mRNAs that had undergone faster deadenylation (Figure 7F). The striking correspondence between the predictions of the model, which had been trained on the continuous-labeling experiment, and the observations of the transcriptional-shutoff experiment validated the

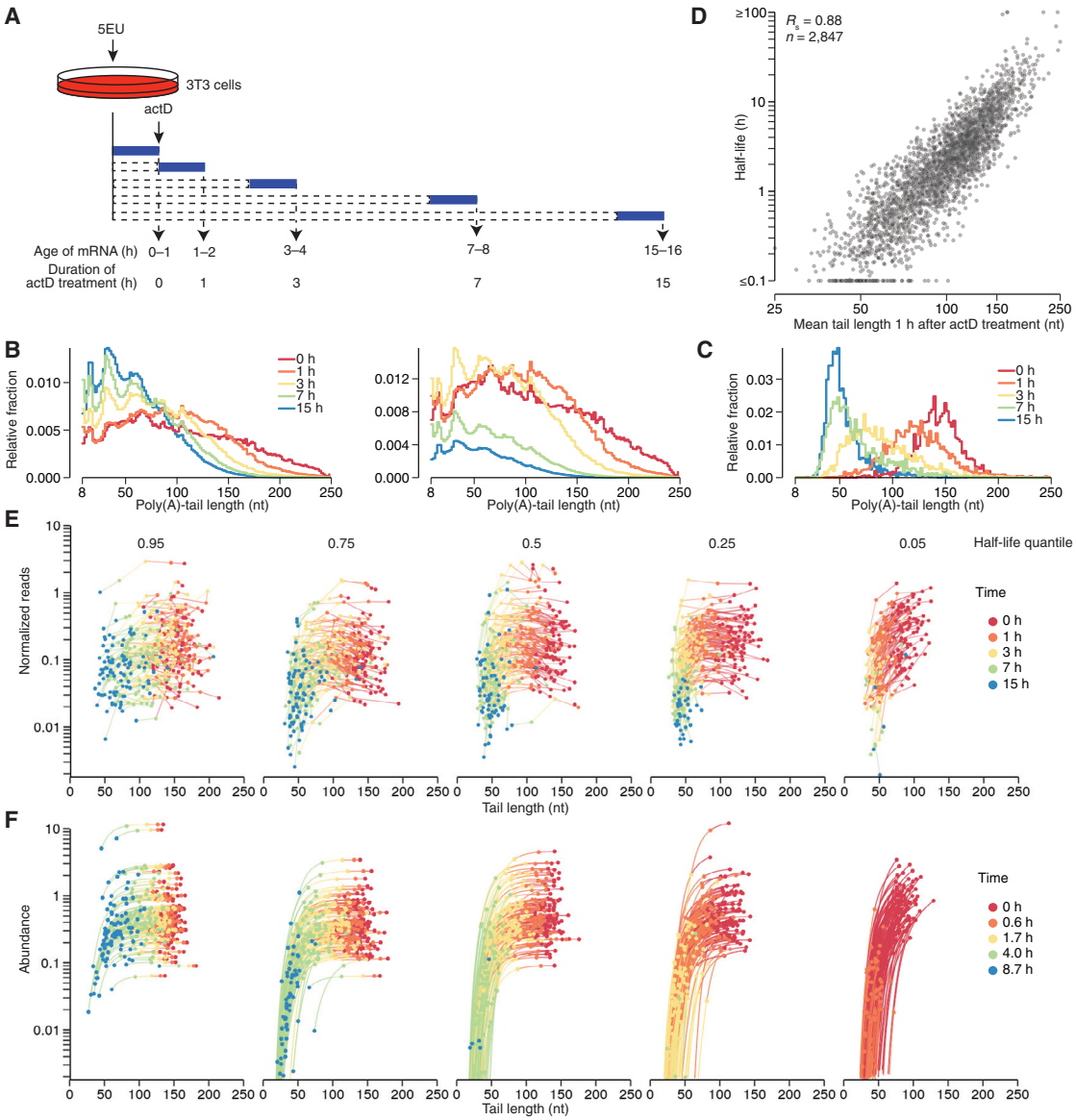

Figure 7. Deadenylation and Decay Dynamics of Synchronous mRNA Populations

(A) Schematic of 5EU metabolic-labeling and actD treatments used to analyze synchronized cellular mRNAs. Cells from cell line 2 were treated for 1 h with 5EU, then treated with actD continuously over a time course spanning 15 h.

(B) Tail-length distributions of labeled mRNA molecules observed at the indicated times after stopping transcription (key). Left: distributions were normalized to all have the same area. Right: distributions were scaled to the abundance of labeled RNAs in each sample and then normalized such that the 0-h time interval had an area of 1. Each bin is 2 nt; results for the bins with tail lengths < 8 nt and ≥ 250 nt are not shown. At 0 h, 7% of the tails were still ≥ 250 nt, which helps explain why the density for the remainder of the tails fell below that observed at 1 h.

(C) Distributions of mean poly(A)-tail lengths for labeled mRNAs of each gene after the indicated duration of transcriptional shutoff. Values for all mRNAs that passed the cutoffs for tail-length measurement at all time points were included (n = 2,155). Each bin is 2 nt.

(D) Relationship between half-life and mean tail length of labeled mRNAs from each gene after 1 h of actD treatment.

(E) Labeled mRNA abundance as a function of mean tail length over time. Results are shown for mRNAs grouped by half-life quantiles (95%, 75%, 50%, 25%, and 5%, left to right, with mRNAs in the 5% bin having the shortest half-lives). Each half-life bin contains 100 genes. mRNA abundance was determined from paired RNA-seq data. Each line connects values for mRNA from a single gene.

(F) Simulation of mRNA abundance as a function of mean tail length over time. For each gene in (E), model parameters fit from the continuous-labeling experiment were used to simulate the initial production of mRNA and its mean tail length from each gene, as well as the fates of these mRNAs and mean tail lengths after production rates were set to 0. Results are plotted as in (E), but using a shorter time course (key) to accommodate the faster dynamics observed without actD. See also Figure S3E.

results and conclusions from both experiments as well as from our analytical framework.

DISCUSSION

Previous studies provide information on deadenylation and degradation dynamics for four mammalian mRNAs and some derivatives, with deadenylation rates reported for two of these four (Mercer and Wake, 1985; Wilson and Treisman, 1988; Shyu et al., 1991; Chen et al., 1995; Gowrishankar et al., 2005; Yamashita et al., 2005). Our study provided a more comprehensive resource for deriving the principles of cytoplasmic mRNA metabolism. Initial analyses revealed unanticipated intra- and intergenic variability in initial tail lengths and indicated that almost all endogenous mRNAs are degraded primarily through deadenylation-linked mechanisms, implying that the deadenylation rate of each mRNA largely determines its half-life with surprisingly little contribution from other mechanisms, such as endonucleolytic cleavage and deadenylation-independent decapping.

Mathematical modeling of our data expanded the known range in deadenylation rate constants from 60-fold to 1000-fold and showed that the link between deadenylation rate and decay generally operates at two levels. First, mRNAs with faster deadenylation rate constants more rapidly reach the short tail lengths associated with destruction of the mRNA body. With respect to the reason that short tail lengths trigger decay, our analyses support the prevailing view that loss of PABPC binding to the poly(A) tail enhances decay, with destabilization beginning as tails become too short for cooperative binding of a PABPC dimer and accelerating as tails become too short for efficient binding of a single PABPC molecule.

A more rapid approach to short-tailed isoforms is not the whole story. mRNAs with identical 20-nt tails but from different genes can have widely different decay rate constants (1000-fold). Moreover, there is a logic to these differences—a logic conferred by the second link between deadenylation rate and decay: mRNAs that had previously undergone more rapid deadenylation decay more rapidly upon reaching short tail lengths. The coherent regulation of deadenylation and short-tailed mRNA decay rates functionally integrates mRNA turnover into a single process to ensure that mRNAs that are rapidly deadenylated are also rapidly cleared from the cell. With respect to mechanism, perhaps changes that occur as mRNA-protein complexes are remodeled to enhance deadenylation also recruit the decapping machinery and its coactivators. Terminal uridylation, which is known to stimulate decapping (Rissland and Norbury, 2009; Morozov et al., 2010; Lim et al., 2014), may aid in this remodeling, as uridylation was preferentially observed on rapidly deadenylated, short-lived mRNAs. Physical connections between the CCR4-NOT deadenylase complex and the decapping complex (Haas et al., 2010; Ozgur et al., 2010; Jonas and Izaurralde, 2015), as well as the intracellular colocalization of these complexes (Parker and Sheth, 2007), presumably also help coordinate deadenylation and short-tailed mRNA decay rates.

The large differences observed for both deadenylation and deadenylation-dependent decay rate constants of mRNAs from different genes raise the question of what mRNA features might specify these differences. MicroRNAs and other factors that help recruit deadenylase complexes typically bind to sites in 3′ UTRs, implying that these sites help to specify the differences (Mauxion et al., 2009; Mühlemann and Lykke-Andersen, 2010; Vlasova-St Louis and Bohjanen, 2011; Van Etten et al., 2012; Fabian et al., 2013; Leppek et al., 2013; Du et al., 2016; Bartel, 2018). However, global analyses of tandem UTR isoforms indicate that the magnitude of the differences conferred by 3′-UTR sequences in NIH 3T3 cells is relatively modest (Spies et al., 2013). Codon composition can also contribute to differences in mRNA stability, but this contribution explains only a small fraction of the variability observed for endogenous mRNAs of mammalian cells (Presnyak et al., 2015; Radhakrishnan et al., 2016; Forrest et al., 2018; Wu et al., 2019). Additional insight will be required to account more fully for the large differences in stabilities observed for different mRNAs. Our results indicate that the focus should be on sequences and processes that influence or correlate with deadenylation rates.

Our global observation that mRNAs typically degrade only after their tail lengths shorten extended to the mammalian transcriptome the notion that exponential decay is not fully appropriate for modeling mRNA degradation (Shyu et al., 1991; Cao and Parker, 2001; Trcek et al., 2011; Deneke et al., 2013). For the exponential model to be appropriate, an mRNA would need to have the same probability of decaying at any point after entering the cytoplasm. In contrast, recently exported, long-tailed mRNAs typically underwent little if any decay, which supported the restricted-degradation model in which mRNAs are provided a discrete time window to function in the cytoplasm. During this window, the body of the mRNA is unaltered, but its age and lifespan are tracked and determined through the action of tail-length dynamics. Nonetheless, for some analyses we used the exponential model and referred to its decay parameter as "half-life" when fitting abundance changes over time because in those cases a more complex model did not provide additional insight, and using mRNA half-lives is still common practice in the field.

Despite the utility of our mathematical model, it did not capture some finer details of mRNA metabolism. For example, it was not designed to model the burst of deadenylation that typically accompanies the loss of each terminal PABPC molecule (Webster et al., 2018). However, when considering the aggregate behavior of multiple mRNAs from the same gene, these bursts become blurred, with some molecules in the burst phase and others between bursts. Accordingly, we fit a single, continuous deadenylation rate constant for the mRNAs of each gene. Likewise, we fit a single, continuous production rate constant for the mRNAs of each gene, despite the known burst behavior of transcription initiation when examined in single cells (Cai et al., 2008).

The uniform deadenylation rate constants of the model were also not suitable for capturing aspects of tail behavior that occurred as tails fell below 20 nt. For example, our analysis of steady-state data revealed buildups of isoforms of short-lived mRNAs at two tail-length ranges: 0–1 and 7–15 nt. A model with uniform deadenylation rate constants can potentially explain a peak at 0 nt but not one at an intermediate tail length, such as 7–15 nt. Recognizing this limitation but still wanting to accurately account for the buildup of isoforms with tails < 20 nt observed for short-lived mRNAs, we fit the abundance of tails < 20 nt by averaging abundance over this length range and

comparing this average to that predicted by the model—an approach that did not require additional parameters to model a buildup of 7–15-nt tails. Such parameters might be warranted if further study shows that the fate of mRNAs with 7–15-nt tails differs from that of mRNAs with 0-nt tails—studies that can be contemplated now that the existence of this buildup is known. Another aspect of mRNA metabolism remaining to be incorporated into a mathematical model is terminal uridylation, which was particularly prominent on short-tailed isoforms of short-lived mRNAs.

A recent study observed that cytoplasmic noncanonical poly(A) polymerases can extend tails, acting on longer-tailed mRNAs and adding mostly A residues but also sometimes generating a mixed tail including a G or another non-A nucleotide (Lim et al., 2018). Because most mRNAs with these mixed tails would not be detected by PAL-seq, these mRNAs would have appeared to have been degraded in our analysis. Thus, our observation of little-to-no degradation of long-tailed mRNAs indicated that, in 3T3 cells, mRNAs with mixed tails comprised only a small fraction of the mRNA molecules at any point in time and did not impact the overall conclusions of our study.

Although our current approach does not model all aspects of mRNA metabolism, there is every reason to believe that the broad behaviors observed in these initial analyses will continue to be observed in more detailed representations of mRNA metabolism. With the acquisition of suitable pre-steady-state data, the dynamics of tail-length changes in the 0–20-nt range, of terminal uridylation, and of cytoplasmic polyadenylation could be better characterized—ultimately enabling incorporation of these phenomena into a comprehensive model of mRNA metabolism. Our methods and analytical framework offer inspiration as well as a foundation for these future efforts.

STAR★METHODS

Detailed methods are provided in the online version of this paper and include the following:

- KEY RESOURCES TABLE
- LEAD CONTACT AND MATERIALS AVAILABILITY
- EXPERIMENTAL MODEL AND SUBJECT DETAILS
  - Cell Lines and Cell Culture
- METHOD DETAILS
  - Metabolic-Labeling Time Courses
  - RNA Standards
  - Biotinylation of 5EU Labeled RNA
  - Purification of Biotinylated RNA
  - PAL-Seq v2
  - PAL-Seq v2 Data Analysis
  - Analysis of PAL-Seq ss-Ligation Data
  - TAIL-Seq
  - RNA-Seq
  - Calculation of mRNA Half-Lives
  - Model of mRNA Metabolism
  - Bootstrap Analysis
  - Background Subtraction for PAL-Seq Data
  - ActD Treatment
- QUANTIFICATION AND STATISTICAL ANALYSIS
- DATA AND CODE AVAILABILITY

SUPPLEMENTAL INFORMATION

Supplemental Information can be found online at https://doi.org/10.1016/j.molcel.2019.12.005.

ACKNOWLEDGMENTS

We thank J. Kwasnieski and other members of the Bartel lab for helpful discussions and the Whitehead Genome Technology Core for high-throughput sequencing. This research was supported by NIH grants GM061835 and GM118135 (D.P.B.) and an NSF Graduate Research Fellowship (T.J.E.). A.O.S. was supported by NIH Medical Scientist Training Program fellowship T32GM007753. D.P.B. is an investigator of the Howard Hughes Medical Institute.

AUTHOR CONTRIBUTIONS

A.O.S., S.W.E., T.J.E., and D.P.B. conceived the project and designed the study. T.J.E., S.W.E., and A.O.S. performed the molecular experiments and analysis. T.J.E. performed the computational modeling with input from K.S.L. and S.E.M. S.W.E., S.G., and T.J.E. adapted PAL-seq for compatibility with current Illumina technologies. K.S.L. and S.W.E. wrote the analysis pipeline for determining tail-length measurements from PAL-seq data. A.O.S., S.W.E., and T.J.E. drafted the manuscript, and T.J.E. and D.P.B. revised the manuscript with input from the other authors.

DECLARATION OF INTERESTS

The authors declare no competing interests.

Received: September 10, 2019
Revised: November 25, 2019
Accepted: December 6, 2019
Published: January 2, 2020

REFERENCES

Baer, B.W., and Kornberg, R.D. (1983). The protein responsible for the repeating structure of cytoplasmic poly(A)-ribonucleoprotein. J. Cell Biol. *96*, 717–721.

Bartel, D.P. (2018). Metazoan MicroRNAs. Cell *173*, 20–51.

Bönisch, C., Temme, C., Moritz, B., and Wahle, E. (2007). Degradation of hsp70 and other mRNAs in Drosophila via the 5′ 3′ pathway and its regulation by heat shock. J. Biol. Chem. *282*, 21818–21828.

Cai, L., Dalal, C.K., and Elowitz, M.B. (2008). Frequency-modulated nuclear localization bursts coordinate gene regulation. Nature *455*, 485–490.

Cao, D., and Parker, R. (2001). Computational modeling of eukaryotic mRNA turnover. RNA *7*, 1192–1212.

Carballo, E., Lai, W.S., and Blackshear, P.J. (2000). Evidence that tristetraprolin is a physiological regulator of granulocyte-macrophage colony-stimulating factor messenger RNA deadenylation and stability. Blood *95*, 1891–1899.

Chang, H., Lim, J., Ha, M., and Kim, V.N. (2014). TAIL-seq: genome-wide determination of poly(A) tail length and 3′ end modifications. Mol. Cell *53*, 1044–1052.

Chen, C.Y., and Shyu, A.B. (1995). AU-rich elements: characterization and importance in mRNA degradation. Trends Biochem. Sci. *20*, 465–470.

Chen, C.Y., Xu, N., and Shyu, A.B. (1995). mRNA decay mediated by two distinct AU-rich elements from c-fos and granulocyte-macrophage colony-stimulating factor transcripts: different deadenylation kinetics and uncoupling from translation. Mol. Cell. Biol. *15*, 5777–5788.

Dahleh, M., Dahleh, M.A., and Verghese, G. (2004). Lectures on dynamic systems and control. A+ A *4*, 1–100. https://ocw.mit.edu/courses/electrical-

engineering-and-computer-science/6-241j-dynamic-systems-and-control-spring-2011/readings/.

Decker, C.J., and Parker, R. (1993). A turnover pathway for both stable and unstable mRNAs in yeast: evidence for a requirement for deadenylation. Genes Dev. *7*, 1632–1643.

Dellavalle, R.P., Petersen, R., and Lindquist, S. (1994). Preferential deadenylation of Hsp70 mRNA plays a key role in regulating Hsp70 expression in Drosophila melanogaster. Mol. Cell. Biol. *14*, 3646–3659.

Deneke, C., Lipowsky, R., and Valleriani, A. (2013). Complex degradation processes lead to non-exponential decay patterns and age-dependent decay rates of messenger RNA. PLoS ONE *8*, e55442.

Dobin, A., Davis, C.A., Schlesinger, F., Drenkow, J., Zaleski, C., Jha, S., Batut, P., Chaisson, M., and Gingeras, T.R. (2013). STAR: ultrafast universal RNA-seq aligner. Bioinformatics *29*, 15–21.

Dölken, L., Ruzsics, Z., Rädle, B., Friedel, C.C., Zimmer, R., Mages, J., Hoffmann, R., Dickinson, P., Forster, T., Ghazal, P., and Koszinowski, U.H. (2008). High-resolution gene expression profiling for simultaneous kinetic parameter analysis of RNA synthesis and decay. RNA *14*, 1959–1972.

Du, H., Zhao, Y., He, J., Zhang, Y., Xi, H., Liu, M., Ma, J., and Wu, L. (2016). YTHDF2 destabilizes m(6)A-containing RNA through direct recruitment of the CCR4-NOT deadenylase complex. Nat. Commun. *7*, 12626.

Eichhorn, S.W., Guo, H., McGeary, S.E., Rodriguez-Mias, R.A., Shin, C., Baek, D., Hsu, S.H., Ghoshal, K., Villén, J., and Bartel, D.P. (2014). mRNA destabilization is the dominant effect of mammalian microRNAs by the time substantial repression ensues. Mol. Cell *56*, 104–115.

Eisen, T.J., Eichhorn, S.W., Subtelny, A.O., and Bartel, D.P. (2020). MicroRNAs cause accelerated decay of short-tailed target mRNAs. Molecular Cell. https://doi.org/10.1016/j.molcel.2019.12.004.

Fabian, M.R., Cieplak, M.K., Frank, F., Morita, M., Green, J., Srikumar, T., Nagar, B., Yamamoto, T., Raught, B., Duchaine, T.F., and Sonenberg, N. (2011). miRNA-mediated deadenylation is orchestrated by GW182 through two conserved motifs that interact with CCR4-NOT. Nat. Struct. Mol. Biol. *18*, 1211–1217.

Fabian, M.R., Frank, F., Rouya, C., Siddiqui, N., Lai, W.S., Karetnikov, A., Blackshear, P.J., Nagar, B., and Sonenberg, N. (2013). Structural basis for the recruitment of the human CCR4-NOT deadenylase complex by tristetraprolin. Nat. Struct. Mol. Biol. *20*, 735–739.

Forrest, M.E., Narula, A., Sweet, T.J., Arango, D., Hanson, G., Ellis, J., Oberdoerffer, S., Coller, J., and Rissland, O.S. (2018). Codon usage and amino acid identity are major determinants of mRNA stability in humans. bioRxiv. https://doi.org/10.1101/488676.

Gowrishankar, G., Winzen, R., Bollig, F., Ghebremedhin, B., Redich, N., Ritter, B., Resch, K., Kracht, M., and Holtmann, H. (2005). Inhibition of mRNA deadenylation and degradation by ultraviolet light. Biol. Chem. *386*, 1287–1293.

Haas, G., Braun, J.E., Igreja, C., Tritschler, F., Nishihara, T., and Izaurralde, E. (2010). HPat provides a link between deadenylation and decapping in metazoa. J. Cell Biol. *189*, 289–302.

Hilgers, V., Teixeira, D., and Parker, R. (2006). Translation-independent inhibition of mRNA deadenylation during stress in Saccharomyces cerevisiae. RNA *12*, 1835–1845.

Hu, J., Li, Y., and Li, P. (2013). MARVELD1 inhibits nonsense-mediated RNA decay by repressing serine phosphorylation of UPF1. PLoS ONE *8*, e68291.

Hunter, J.D. (2007). Matplotlib: A 2D graphics environment. Comput. Sci. Eng. *9*, 90–95.

Jan, C.H., Friedman, R.C., Ruby, J.G., and Bartel, D.P. (2011). Formation, regulation and evolution of Caenorhabditis elegans 3'UTRs. Nature *469*, 97–101.

Jao, C.Y., and Salic, A. (2008). Exploring RNA transcription and turnover in vivo by using click chemistry. Proc. Natl. Acad. Sci. USA *105*, 15779–15784.

Jia, H., Wang, X., Liu, F., Guenther, U.P., Srinivasan, S., Anderson, J.T., and Jankowsky, E. (2011). The RNA helicase Mtr4p modulates polyadenylation in the TRAMP complex. Cell *145*, 890–901.

Jonas, S., and Izaurralde, E. (2015). Towards a molecular understanding of microRNA-mediated gene silencing. Nat. Rev. Genet. *16*, 421–433.

Kwak, J.E., and Wickens, M. (2007). A family of poly(U) polymerases. RNA *13*, 860–867.

Leppek, K., Schott, J., Reitter, S., Poetz, F., Hammond, M.C., and Stoecklin, G. (2013). Roquin promotes constitutive mRNA decay via a conserved class of stem-loop recognition motifs. Cell *153*, 869–881.

Li, H., Handsaker, B., Wysoker, A., Fennell, T., Ruan, J., Homer, N., Marth, G., Abecasis, G., Durbin, R., and Genome Project Data Processing, S. (2009). The Sequence Alignment/Map format and SAMtools. Bioinformatics *25*, 2078–2079.

Lim, J., Ha, M., Chang, H., Kwon, S.C., Simanshu, D.K., Patel, D.J., and Kim, V.N. (2014). Uridylation by TUT4 and TUT7 marks mRNA for degradation. Cell *159*, 1365–1376.

Lim, J., Lee, M., Son, A., Chang, H., and Kim, V.N. (2016). mTAIL-seq reveals dynamic poly(A) tail regulation in oocyte-to-embryo development. Genes Dev. *30*, 1671–1682.

Lim, J., Kim, D., Lee, Y.S., Ha, M., Lee, M., Yeo, J., Chang, H., Song, J., Ahn, K., and Kim, V.N. (2018). Mixed tailing by TENT4A and TENT4B shields mRNA from rapid deadenylation. Science *361*, 701–704.

Lima, S.A., Chipman, L.B., Nicholson, A.L., Chen, Y.H., Yee, B.A., Yeo, G.W., Coller, J., and Pasquinelli, A.E. (2017). Short poly(A) tails are a conserved feature of highly expressed genes. Nat. Struct. Mol. Biol. *24*, 1057–1063.

Mauxion, F., Chen, C.Y., Séraphin, B., and Shyu, A.B. (2009). BTG/TOB factors impact deadenylases. Trends Biochem. Sci. *34*, 640–647.

Mercer, J.F., and Wake, S.A. (1985). An analysis of the rate of metallothionein mRNA poly(A)-shortening using RNA blot hybridization. Nucleic Acids Res. *13*, 7929–7943.

Mor, A., Suliman, S., Ben-Yishay, R., Yunger, S., Brody, Y., and Shav-Tal, Y. (2010). Dynamics of single mRNP nucleocytoplasmic transport and export through the nuclear pore in living cells. Nat. Cell Biol. *12*, 543–552.

Morozov, I.Y., Jones, M.G., Razak, A.A., Rigden, D.J., and Caddick, M.X. (2010). CUCU modification of mRNA promotes decapping and transcript degradation in Aspergillus nidulans. Mol. Cell. Biol. *30*, 460–469.

Mühlemann, O., and Lykke-Andersen, J. (2010). How and where are nonsense mRNAs degraded in mammalian cells? RNA Biol. *7*, 28–32.

Muhlrad, D., Decker, C.J., and Parker, R. (1994). Deadenylation of the unstable mRNA encoded by the yeast MFA2 gene leads to decapping followed by 5′–>3′ digestion of the transcript. Genes Dev. *8*, 855–866.

Nelson, J.O., Moore, K.A., Chapin, A., Hollien, J., and Metzstein, M.M. (2016). Degradation of Gadd45 mRNA by nonsense-mediated decay is essential for viability. eLife *5*, e12876.

Nocedal, J. (1980). Updating Quasi-Newton Matrices with Limited Storage. Math Comput *35*, 773–782.

Oliphant, T.E. (2007). Python for scientific computing. Comput. Sci. Eng. *9*, 10–20.

Ozgur, S., Chekulaeva, M., and Stoecklin, G. (2010). Human Pat1b connects deadenylation with mRNA decapping and controls the assembly of processing bodies. Mol. Cell. Biol. *30*, 4308–4323.

Palatnik, C.M., Storti, R.V., and Jacobson, A. (1979). Fractionation and functional analysis of newly synthesized and decaying messenger RNAs from vegetative cells of Dictyostelium discoideum. J. Mol. Biol. *128*, 371–395.

Park, E., and Maquat, L.E. (2013). Staufen-mediated mRNA decay. Wiley Interdiscip. Rev. RNA *4*, 423–435.

Parker, R., and Sheth, U. (2007). P bodies and the control of mRNA translation and degradation. Mol. Cell *25*, 635–646.

Pedregosa, F., Varoquaux, G., Gramfort, A., Michel, V., Thirion, B., Grisel, O., Blondel, M., Prettenhofer, P., Weiss, R., Dubourg, V., et al. (2011). Scikit-learn: Machine learning in Python. J. Mach. Learn. Res. *12*, 2825–2830.

Presnyak, V., Alhusaini, N., Chen, Y.H., Martin, S., Morris, N., Kline, N., Olson, S., Weinberg, D., Baker, K.E., Graveley, B.R., and Coller, J. (2015). Codon optimality is a major determinant of mRNA stability. Cell *160*, 1111–1124.

Quinlan, A.R., and Hall, I.M. (2010). BEDTools: a flexible suite of utilities for comparing genomic features. Bioinformatics *26*, 841–842.

Rabani, M., Levin, J.Z., Fan, L., Adiconis, X., Raychowdhury, R., Garber, M., Gnirke, A., Nusbaum, C., Hacohen, N., Friedman, N., et al. (2011). Metabolic labeling of RNA uncovers principles of RNA production and degradation dynamics in mammalian cells. Nat. Biotechnol. *29*, 436–442.

Radhakrishnan, A., Chen, Y.H., Martin, S., Alhusaini, N., Green, R., and Coller, J. (2016). The DEAD-Box protein Dhh1p couples mRNA decay and translation by monitoring codon optimality. Cell *167*, 122–132.e9.

R Core Team (2019). R: A language and environment for statistical computing (R Foundation for Statistical Computing).

Rissland, O.S., and Norbury, C.J. (2009). Decapping is preceded by 3′ uridylation in a novel pathway of bulk mRNA turnover. Nat. Struct. Mol. Biol. *16*, 616–623.

Rissland, O.S., Mikulasova, A., and Norbury, C.J. (2007). Efficient RNA polyuridylation by noncanonical poly(A) polymerases. Mol. Cell. Biol. *27*, 3612–3624.

Schwanhäusser, B., Busse, D., Li, N., Dittmar, G., Schuchhardt, J., Wolf, J., Chen, W., and Selbach, M. (2011). Global quantification of mammalian gene expression control. Nature *473*, 337–342.

Shav-Tal, Y., Darzacq, X., Shenoy, S.M., Fusco, D., Janicki, S.M., Spector, D.L., and Singer, R.H. (2004). Dynamics of single mRNPs in nuclei of living cells. Science *304*, 1797–1800.

Sheiness, D., and Darnell, J.E. (1973). Polyadenylic acid segment in mRNA becomes shorter with age. Nat. New Biol. *241*, 265–268.

Shyu, A.B., Belasco, J.G., and Greenberg, M.E. (1991). Two distinct destabilizing elements in the c-fos message trigger deadenylation as a first step in rapid mRNA decay. Genes Dev. *5*, 221–231.

Soetaert, K., Petzoldt, T., and Setzer, R.W. (2010). Solving Differential Equations in R. R J *2*, 5-15.

Spies, N., Burge, C.B., and Bartel, D.P. (2013). 3′ UTR-isoform choice has limited influence on the stability and translational efficiency of most mRNAs in mouse fibroblasts. Genome Res. *23*, 2078–2090.

Subtelny, A.O., Eichhorn, S.W., Chen, G.R., Sive, H., and Bartel, D.P. (2014). Poly(A)-tail profiling reveals an embryonic switch in translational control. Nature *508*, 66–71.

Tani, H., Imamachi, N., Salam, K.A., Mizutani, R., Ijiri, K., Irie, T., Yada, T., Suzuki, Y., and Akimitsu, N. (2012). Identification of hundreds of novel UPF1 target transcripts by direct determination of whole transcriptome stability. RNA Biol. *9*, 1370–1379.

Trcek, T., Larson, D.R., Moldón, A., Query, C.C., and Singer, R.H. (2011). Single-molecule mRNA decay measurements reveal promoter- regulated mRNA stability in yeast. Cell *147*, 1484–1497.

Tullai, J.W., Schaffer, M.E., Mullenbrock, S., Sholder, G., Kasif, S., and Cooper, G.M. (2007). Immediate-early and delayed primary response genes are distinct in function and genomic architecture. J. Biol. Chem. *282*, 23981–23995.

Van Etten, J., Schagat, T.L., Hrit, J., Weidmann, C.A., Brumbaugh, J., Coon, J.J., and Goldstrohm, A.C. (2012). Human Pumilio proteins recruit multiple deadenylases to efficiently repress messenger RNAs. J. Biol. Chem. *287*, 36370–36383.

Vlasova-St Louis, I., and Bohjanen, P.R. (2011). Coordinate regulation of mRNA decay networks by GU-rich elements and CELF1. Curr. Opin. Genet. Dev. *21*, 444–451.

Webster, M.W., Chen, Y.H., Stowell, J.A.W., Alhusaini, N., Sweet, T., Graveley, B.R., Coller, J., and Passmore, L.A. (2018). mRNA deadenylation is coupled to translation rates by the differential activities of Ccr4-Not nucleases. Mol. Cell *70*, 1089–1100.e8.

Wickham, H., Averick, M., Bryan, J., Chang, W., McGowan, L.D.A., François, R., Grolemund, G., Hayes, A., Henry, L., Hester, J., et al. (2019). Welcome to the Tidyverse. J. Open Source Softw. *4*, 1686.

Wilson, T., and Treisman, R. (1988). Removal of poly(A) and consequent degradation of c-fos mRNA facilitated by 3′ AU-rich sequences. Nature *336*, 396–399.

Wu, Q., Medina, S.G., Kushawah, G., DeVore, M.L., Castellano, L.A., Hand, J.M., Wright, M., and Bazzini, A.A. (2019). Translation affects mRNA stability in a codon-dependent manner in human cells. eLife *8*, e45396.

Yamashita, A., Chang, T.C., Yamashita, Y., Zhu, W., Zhong, Z., Chen, C.Y., and Shyu, A.B. (2005). Concerted action of poly(A) nucleases and decapping enzyme in mammalian mRNA turnover. Nat. Struct. Mol. Biol. *12*, 1054–1063.

Yi, H., Park, J., Ha, M., Lim, J., Chang, H., and Kim, V.N. (2018). PABP cooperates with the CCR4-NOT complex to promote mRNA deadenylation and block precocious decay. Mol. Cell *70*, 1081–1088.e5.

STAR★METHODS

KEY RESOURCES TABLE

REAGENT or RESOURCE	SOURCE	IDENTIFIER
Chemicals, Peptides, and Recombinant Proteins		
cOmplete Mini EDTA-free Protease Inhibitor tablets	Roche	Cat# 4693159001
TRI Reagent	Ambion	Cat# AM9738
Bovine Calf Serum	Sigma	Cat# 12133C
5-ethynyluridine	Jena Biosciences	Cat# CLK-N002-10
Vaccinia capping system	NEB	Cat# M2080S
SUPERaseIn	Thermo Fisher	Cat# AM2694
T4 polynucleotide kinase	NEB	Cat# M0201S
MEGAscript T7	Thermo Fisher	Cat# AM1333
5-ethynyluridine-triphosphate	Jena Biosciences	Cat# CLK-T08
Oligo(dT) Dynabeads	Thermo Fisher	Cat# 61002
Disulfide biotin azide	Click Chemistry Tools	Cat# 1168-10
Tris(3-hydroxypropyltriazolylmethyl)amine	Click Chemistry Tools	Cat# 1010-100
Sodium Ascorbate	Sigma	Cat# 11140
Dynabeads MyOne Streptavidin C1 beads	Thermo Fisher	Cat# 65001
Yeast total RNA	Thermo Fisher	Cat# AM7118
Tris(2-carboxyethyl)phosphine	Sigma	Cat# 646547
RNase T1	Thermo Fisher	Cat# AM2283
Superscript III Reverse Transcriptase	Invitrogen	Cat# 18080044
Titanium Taq Polymerase	Takara	Cat# 639208
AMPure beads	Beckman Coulter	Cat# NC9933872
RiboZero Gold HMR	Illumina	Cat# MRZG12324
T4 RNA ligase I	NEB	Cat# M0437
T4 RNA ligase II, truncated KQ	NEB	Cat# M0373
HT2 hybridization buffer	Illumina	HT2
dTTP	Thermo Fisher	Cat# R0171
[γ-^{32}P]ATP	Perkin Elmer	Cat# NEG035C001MC
[α-^{32}P]GTP	Perkin Elmer	Cat# NEG006H500UC
Critical Commercial Assays		
Micro Bio-Spin P30 gel columns	Bio-Rad	7326250
Deposited Data		
Fragmented RNAseq	This study	GEO: GSE134660
PAL-seq	This study	GEO: GSE134660
Experimental Models: Cell Lines		
Mouse: miR-1–inducible 3T3 cell line	Eichhorn et al., 2014	N/A
Mouse: miR-155–inducible 3T3 cell line	Eichhorn et al., 2014	N/A
Oligonucleotides		
See Table S3	This paper	N/A
Library preparation adapters and primers (also listed in Table S3)	IDT	N/A
RNA standards (also listed in Table S3)	Subtelny et al., 2014	N/A

(*Continued on next page*)

Continued

REAGENT or RESOURCE	SOURCE	IDENTIFIER
Software and Algorithms		
R 3.6.1	The R Foundation for Statistical Computing	https://www.r-project.org/foundation/
Python	The Python Software Foundation	https://www.python.org/; RRID: SCR_008394
Matplotlib 2.0.0	Hunter, 2007	https://matplotlib.org/; RRID: SCR_008624
Numpy 1.14.3	Oliphant, 2007	https://numpy.org; RRID: SCR_008633
Scipy 1.0.1	Oliphant, 2007	https://www.scipy.org; RRID: SCR_008058
scikit-learn 0.18.1	Pedregosa et al., 2011	https://scikit-learn.org/stable/; RRID: SCR_002577
Hmmlearn 0.2.0	Hmmlearn developers, 2010	https://hmmlearn.readthedocs.io/en/latest/
Ghmm	Alexander Schliep	http://ghmm.org/
STAR v2.5.4b	Dobin et al., 2013	RRID: SCR_015899
Bedtools v2.26.0	Quinlan and Hall, 2010	RRID: SCR_006646
Samtools	Li et al., 2009	RRID: SCR_002105
Tail kinetics model	This study	https://github.com/timeisen/DynamicsOfCytoplasmicMrnaMetabolism
Exponential decay model	This study	https://github.com/timeisen/DynamicsOfCytoplasmicMrnaMetabolism
Tail length determination for splint-ligation data	This study	https://github.com/kslin/PAL-seq
Tail length determination for single-stranded ligation data	This study	https://github.com/kslin/PAL-seq
Flow cell configuration for a HiSeq2500 running PALseq	This study	https://github.com/kslin/PAL-seq
L-BFGS-B optimization algorithm	Nocedal, 1980	http://www.uivt.cas.cz/~luksan/subroutines.html
deSolve v1.21	Soetaert et al., 2010	https://cran.r-project.org/web/packages/deSolve/citation.html
NLopt v1.0.4	Steven G. Johnson, The NLopt nonlinear-optimization package.	https://nlopt.readthedocs.io/en/latest/
Tidyverse v1.2.1	Wickham et al., 2019	https://www.tidyverse.org/

LEAD CONTACT AND MATERIALS AVAILABILITY

Further information and requests for resources and reagents should be directed to and will be fulfilled by the Lead Contact, David Bartel (dbartel@wi.mit.edu).

EXPERIMENTAL MODEL AND SUBJECT DETAILS

Cell Lines and Cell Culture

Clonal 3T3 cell lines engineered to express miR-155 (cell line 1) or miR-1 (cell line 2) upon doxycycline treatment were previously described (Eichhorn et al., 2014). Cells were grown at 37°C in 5% CO_2 in DMEM supplemented with 10% BCS (Sigma-Aldrich) and 2 μg/mL puromycin. 3T3 cells are male. Mycoplasma testing was performed and no contamination was observed.

METHOD DETAILS

Metabolic-Labeling Time Courses

Cells from each line were plated onto 500 cm^2 plates at 6.6 million cells per plate and cultured for two days such that they reached ~70%–80% confluency, at which point growth media was supplemented with 5-ethynyl uridine (5EU, Jena Biosciences) (Jao and Salic, 2008) at a final concentration of 400 μM. After the desired labeling intervals cells were harvested (Figure 1A). Four plates were harvested for each 40 min time interval, three plates for each 1 h time interval, and two plates for each other time interval. A plate that had never received 5EU was harvested in parallel for each condition.

Cells were harvested at 4°C, washed twice with 50 mL ice-cold PBS, pH 7.3 containing 100 μg/mL cycloheximide and then used to prepare cytoplasmically enriched lysate as described (Subtelny et al., 2014). An aliquot of cleared lysate was flash frozen for use in ribosome profiling (Eisen et al., 2020), and the rest of the lysate was added to 5 volumes of TRI reagent (Ambion) and frozen at –80°C. Samples stored in TRI reagent were thawed at room temperature, and RNA was purified according to the manufacturer's protocol and used for RNA-seq or PAL-seq v2.

RNA Standards

Two sets of tail-length standards (set 1 and set 3, Table S3) were described previously (standard mix 2 and standard mix 1) (Subtelny et al., 2014). The other set of standards (set 2, Table S3) was prepared based on a 705 nt fragment of the *Renilla* luciferase mRNA, which was transcribed and gel purified as described (Subtelny et al., 2014) and then capped using a Vaccinia capping system (2000 μL reaction containing 500 μg RNA, 1000 U Vaccinia capping enzyme (NEB), 1X Capping Buffer (NEB), 0.1 mM S-adenosyl methionine, 0.5 mM GTP, 50 nM [α–^{32}P]-GTP, 2000 U SUPERaseIn (ThermoFisher) at 37°C for 1 h), monitoring the amount of incorporated radioactivity to ensure that capping was quantitative. Following the capping reaction, the 2′,3′ cyclic phosphate at the 3′ end was removed using T4 polynucleotide kinase (Subtelny et al., 2014). The capped, dephosphorylated product was joined by splinted ligation to each of seven different poly(A)-tailed barcode oligonucleotides (Subtelny et al., 2014). These seven 3′ ligation partners included 110 and 210 nt poly(A) oligonucleotides prepared as described (Subtelny et al., 2014), and five gel-purified synthetic oligonucleotides (IDT), one with a 10 nt poly(A) tract and the other four with a 29 nt poly(A) tract followed by either A, C, G, or U. Ligation products were gel purified, mixed in desired ratios, with the final ratios of the different-sized species confirmed by analysis on a denaturing polyacrylamide gel.

Short and long standards were used to monitor enrichment of 5EU-containing fragmented RNA or non-fragmented RNA, respectively. Short 5EU standards were prepared by *in vitro* transcription of annealed DNA oligos to produce a 30 nt and 40 nt RNA, with the latter containing a single 5EU (Table S3). *In vitro* transcription was performed with the MEGAscript T7 transcription kit (ThermoFisher) according to the manufacturer's protocol, except UTP was replaced with 5-ethynyluridine-triphosphate (Jena Biosciences) when transcribing the 40 nt RNA. Long standards were prepared by *in vitro* transcription of sequences encoding firefly luciferase and GFP using the MEGAscript T7 transcription kit and 0.1 μM PCR product as the template. When transcribing *GFP* RNA, a 20:1 ratio of UTP to 5-ethynyluridine-triphosphate was used. Short and long standards were gel purified and stored at –80°C. Prior to use, a portion of each standard was cap-labeled and gel purified again, which enabled measurement of the recovery of the 5EU-containing standard relative to that of the uridine-only standard.

Three 28–30 nt RNAs (Table S3) were synthesized (IDT) for use as quantification standards in RNA-seq. These standards were gel purified, and 0.1 fmol of each was added to each sample immediately prior to library preparation.

Biotinylation of 5EU Labeled RNA

The RNA-seq libraries analyzed in this study were from fragmented RNAs, size selected to match ribosome-profiling libraries (Eisen et al., 2020). For these libraries, poly(A) RNA was purified from 50 μg total RNA of the 40 min, 1, 2, and 4 h samples and 25 μg total RNA of the 8 h sample using oligo(dT) Dynabeads (ThermoFisher) according to manufacturer's protocol. RNA was fragmented and 27–33 nt fragments were isolated as described (Subtelny et al., 2014) and short standards that monitored 5EU enrichment were added. Biotinylation was performed in the presence of a Cu(II) catalyst in a 20 μL reaction containing 50 mM HEPES, pH 7.5, 4 mM disulfide biotin azide (Click Chemistry Tools), 2.5 mM $CuSO_4$, 2.5 mM Tris(3-hydroxypropyltriazolylmethyl)amine (THPTA, Sigma-Aldrich), and 10 mM sodium ascorbate (Sigma-Aldrich), incubated at room temperature for 1 h. Reactions were stopped with 5 mM EDTA and then extracted with phenol–chloroform (pH 8.0). For the steady-state samples, 5 μg of RNA from the 40 min sample was poly(A) selected and fragmented, and 27–33 nt fragments were size selected and carried forward without enriching for 5EU.

For PAL-seq v2, long standards used to monitor 5EU enrichment and recovery were added to total RNA (using a 1:10 ratio of 5EU-containing standard to non-5EU-containing standard), and samples were click labeled as above in reactions with 2.5 μg/μL RNA. For samples from the cell line 1 time course, click reactions were performed with 500, 500, 250, 200, or 100 μg total RNA for the 40 min, 1 h, 2 h, 4 h, or 8 h samples. For samples from the cell line 2 time course, click reactions were performed with 800, 525, 350, or 200 μg total RNA for the 40 min, 1 h, 2 h, or 4 h, respectively. For both cell lines, the steady-state samples did not undergo biotinylation or pull-down.

Purification of Biotinylated RNA

For RNA-seq, Dynabeads MyOne Streptavidin C1 beads (ThermoFisher) for each set of samples were combined and batch washed, starting with 200 μL of beads per reaction. Beads were washed twice with 1X B&W buffer (5 mM Tris-HCl, pH 7.5, 0.5 mM EDTA, 1 M NaCl and 0.005% Tween-20), twice with solution A (0.1 M NaOH, 50 mM NaCl), twice with solution B (0.1 M NaCl), and then twice with water, using for each wash a volume equal to that of the initial bead suspension. Following the last wash, beads were resuspended in an initial bead volume of 1X high salt wash buffer (HSWB, 10 mM Tris-HCl, pH 7.4, 1 mM EDTA, 0.1 M NaCl, 0.01% Tween-20) supplemented with 0.5 mg/mL yeast RNA (ThermoFisher) and incubated at room temperature for 30 min with end-over-end rotation, again using a volume equal to that of the initial bead suspension. Beads were then washed three times with 200 μL 1X HSWB per reaction and split for each reaction during the last wash. After the wash was removed, sample RNA resuspended in 200 μL 1X HSWB was added to blocked beads and incubated with end-over-end rotation at room temperature for 30 min. Beads were washed

twice with 800 μL water at 50°C, incubating at 50°C for 2 min for each wash, and then twice with 800 μL 10X HSWB. RNA was eluted from beads by incubating with 200 μL 0.5 M tris(2-carboxyethyl)phosphine (TCEP, Sigma-Aldrich) at 50°C for 20 min with end-over-end rotation. The initial eluate was collected, and beads were resuspended in 150 μL water and eluted again, combining the two eluates for each sample. RNA from the eluate was then ethanol precipitated using linear acrylamide as a carrier.

Purifications of non-fragmented RNA were performed as above, except bead volumes were adjusted based on estimates of the amount of labeled RNA in each sample. For the cell line 1 samples, 292, 431, 410, 598, and 500 μL of beads were used for the 40 min, 1 h, 2 h, 4 h, and 8 h samples, respectively. For the cell line 2 samples, 467, 452, 575, and 598 μL streptavidin beads were used for the 40 min, 1 h, 2 h, and 4 h samples, respectively.

Pilot experiments designed to optimize the 5EU biotinylation and purification confirmed that RNAs containing at least one 5EU could be purified efficiently, with over 80% of a model RNA substrate containing a single 5EU becoming biotinylated in a 1 h reaction (Eisen et al., 2020). This high reaction efficiency was important for the RNA-seq samples, as RNA fragments from these libraries, generated to match ribosome-profiling samples (Eisen et al., 2020), were only ~30 nt long and estimated to typically contain at most a single 5EU. Indeed, for each of the three protocols, which started with either full-length RNA (PAL-seq) or fragmented RNA (RNA-seq), metabolically labeled RNA was substantially enriched above background (Eisen et al., 2020).

PAL-Seq v2

This method starts with the same mRNA workup as the initial version of PAL-seq (Subtelny et al., 2014), except the design of the 3′ adaptor allows for ligation to tails ending with a uridine nucleotide, as implemented in an improved version of TAIL-seq (Lim et al., 2016). PAL-seq v2 also includes a primer-extension reaction that occurs on the Illumina flowcell, with the goal of extending the sequencing primer all of the way through the poly(A) tail, so that the first sequencing read identifies both the mRNA and its cleavage-and-polyadenylation site, as in PAL-seq v1 (Subtelny et al., 2014). After stripping the extended primer, the poly(A)-tail length is then measured by direct sequencing of the poly(A) tail, as in TAIL-seq (Chang et al., 2014) (Figure S1A).

We used RNA standards of defined tail lengths to monitor library preparation, sequencing, and the computational pipeline for improved versions of PAL-seq and our implementation of TAIL-seq. Depletion of long-tailed sequences was the most prevalent source of measurement error. For TAIL-seq, this depletion seemed highly dependent on the sequencing protocol, with the best results obtained on a HiSeq machine in high-output mode using the v3 reagent kit.

Steady-state RNA (25 μg of unselected RNA from the 40 min sample) or half of the RNA eluted from each 5EU-selected sample was used to prepare PAL-seq libraries. Tail-length standard mixes (1 ng of set 1 and 2 ng of set 2 for each 5EU-selected sample, and twice these amounts for the steady-state sample), and trace 5′-radiolabeled marker RNAs (Table S3) were added to each sample to assess tail-length measurements and ligation outcomes, respectively. Polyadenylated ends including those with a terminal uridine were ligated to a 3′-biotinylated adaptor DNA oligonucleotide (1.8 μM) in the presence of two splint DNA oligonucleotides (1.25 μM and 0.25 μM for the U and A-containing splint oligos, respectively, Table S3) using T4 Rnl2 (NEB) in an overnight reaction at 18°C. Following 3′-adaptor ligation the RNA was extracted with phenol–chloroform (pH 8.0), precipitated, resuspended in 1X RNA T1 sequence buffer (ThemoFisher), heated to 50°C for 5 min and then put on ice. RNase T1 was then added to a final concentration of 0.006 U/μL, and the reaction was incubated at room temperature for 30 min, followed by phenol–chloroform extraction and RNA precipitation. Precipitated RNA was captured on streptavidin beads, 5′ phosphorylated, and ligated to a 5′ adaptor as described (Subtelny et al., 2014) but using a modified 5′ adaptor sequence (Table S3). Following reverse transcription using SuperScript III (Invitrogen) with a barcode-containing DNA primer, cDNA was purified as described (Subtelny et al., 2014), except a 160–810 nt size range was selected. Libraries were amplified by PCR for 8 cycles using Titanium Taq (Takara) polymerase according to the manufacturer's protocol with a 1.5 min combined annealing/extension step at 57°C. PCR-amplified libraries were purified using AMPure beads (Agencourt, 40 μL beads per 50 μL PCR, two rounds of purification) according to the manufacturer's instructions.

The use of a splinted ligation of the 3′ adaptor to the poly(A) tail had the advantage of specifically ligating to mRNAs without the need to deplete ribosomal or other abundant RNAs. However, this approach was not suitable for acquiring measurements for mRNAs with tails that were either very short (< 8 nt) or extended by more than one uridine, because such tails would ligate less efficiently (or not at all) when using a splinted ligation to the 3′ adaptor. To account for these mRNAs with either very short or highly modified tails, we implemented a protocol that used single-stranded (ss) ligation and different mRNA enrichment steps to prepared libraries from steady-state RNA isolated from each of the two cell lines. For each sample, 5 μg of total RNA was depleted of rRNA using RiboZero Gold HMR (Illumina) and further depleted of the 5.8S rRNA by subtractive hybridization. Subtractive hybridization was performed by mixing 2x SSC buffer (3M sodium chloride, 300mM sodium citrate, pH 7.0), total RNA, and 4.8 μM of each 5.8S subtractive-hybridization oligo (Table S3) in a 50 μL reaction, heating the reaction to 70°C for 5 min, then cooling it at 1°C/min to 37°C to anneal the oligos to the RNA. During this cooling, 250 μL of Dynabeads MyOne Streptavidin C1 beads per sample (ThermoFisher) were washed twice with 1X B&W buffer (5 mM Tris-HCl, pH 7.5, 0.5 mM EDTA, 1 M NaCl and 0.005% Tween-20), twice with solution A (0.1 M NaOH, 50 mM NaCl), twice with solution B (0.1 M NaCl), and then resuspended in 50 μL of 2X B&W buffer. After cooling, the entire 50 μL RNA/oligo mixture was added to 50 μL of washed beads, then incubated at room temperature for 15 min with end-over-end rotation. The sample was then magnetized and the supernatant was withdrawn and precipitated by adding 284 μL of water, 4 μL of 5 mg/mL linear acrylamide, and 1 mL of ice-cold 96% ethanol. After resuspension, RNA was ligated to a 3′ adaptor containing four random-sequence nucleotides and an adenylyl group at its 5′ end (Table S3) in a 70 μl reaction containing 10 μM adaptor, 1X T4 RNA Ligase Reaction Buffer (NEB), 20 U/μL T4 RNA Ligase 2 truncated KQ (NEB), 0.3 U/μL SUPERaseIn (ThermoFisher), and 20% PEG 8000. The

reaction was incubated at 22°C overnight and then stopped by addition of EDTA (3.5 mM final concentration after bringing the reaction to 400 μL with water). RNA was phenol–chloroform extracted, precipitated, and subsequent library preparation was as for the splinted-ligation libraries.

PAL-seq v2 libraries were sequenced on an Illumina HiSeq 2500 operating in rapid mode. Hybridization mixes were prepared with 0.375 fmol PCR-amplified library that had been denatured with standard NaOH treatment and brought to a final volume of 125 μL with HT1 hybridization buffer (Illumina, 3 pM library in final mix). Following standard cluster generation and sequencing-primer hybridization, two dark cycles were performed for the splinted-ligation libraries (i.e., two rounds of standard sequencing-by-synthesis in which imaging was skipped), which extended the sequencing primer by 2 nt, thereby enabling measurement of poly(A) tails terminating in non-adenosine bases. For the direct-ligation libraries, six dark cycles were performed instead of two, which extended the sequencing primer past the four random-sequence nucleotides in the 3′ adaptor and the last two residues of the tail.

Following the two dark cycles, a custom primer-extension reaction was performed on the sequencer using 50 μM dTTP as the only nucleoside triphosphate in the reaction. To perform this extension, the flow cell temperature was first set to 20°C. Then, 120 μL of universal sequencing buffer (USB, Illumina) was flowed over each lane, followed by 150 μL of Klenow buffer (NEB buffer 2 supplemented with 0.02% Tween-20). Reaction mix (Klenow buffer, 50 μM dTTP, and 0.1 U/μL Large Klenow Fragment, NEB) was then flowed on in two aliquots (150 μL and 100 μL). The flow-cell temperature was then increased to 37°C at a rate of 8.5°C per min and the incubation continued another 2 min after reaching 37°C. 150 μL of fresh reaction mix was then flowed in, and following a 2 min incubation, 75 μL of reaction mix was flowed in eight times, with each flow followed by a 2 min incubation. The reaction was stopped by decreasing the flow cell temperature to 20°C, flowing in 150 μL of quench buffer (Illumina HT2 buffer supplemented with 10 mM EDTA) and then washing with 75 μL of HT2 buffer. The flow cell was prepared for subsequent sequencing with a 150 μL and a 75 μL flow of HT1 buffer (Illumina). 50 cycles of standard sequencing-by-synthesis were then performed to yield the first sequencing read (read 1). XML files used for this protocol are provided at https://github.com/kslin/PAL-seq.

The flow cell was stripped, a barcode sequencing primer was annealed, and seven cycles of standard sequencing-by-synthesis were performed to read the barcode. The flow cell was then stripped again, and the same primer as used for read 1 was hybridized and used to prime 250 cycles of standard sequencing-by-synthesis to generate read 2. Thus, each PAL-seq tag consisted of three reads: read 1, read 2, and the indexing (barcode) read. For cases in which a tag corresponded to a polyadenylated mRNA, read 1 was the reverse complement of the 3′ end of the mRNA immediately 5′ of the poly(A) tail and was used to identify the mRNA and cleavage-and-polyadenylation site of long-tailed mRNAs. The indexing read was used to identify the sample, and read 2 was used to measure poly(A)-tail length and identify the mRNA and cleavage-and-polyadenylation site of short-tailed mRNAs. The intensity files of reads 1 and 2 were used for poly(A)-tail length determination, along with the Illumina fastq files.

PAL-Seq v2 Data Analysis

Tail lengths for the splinted-ligation data were determined using a Gaussian hidden Markov model (GHMM) from the python2.7 package ghmm (http://ghmm.org/), analogous to the model used in TAIL-seq (Chang et al., 2014) and described in the next paragraph. Read 1 was mapped using STAR (v2.5.4b) run with the parameters '–alignIntronMax 1–outFilterMultimapNmax 1–outFilterMismatchNoverLmax 0.04–outFilterIntronMotifs RemoveNoncanonicalUnannotated–outSJfilterReads', aligning to an index of the mouse genome built using mm10 transcript annotations that had been compressed to unique instances of each gene selecting the longest transcript and removing all overlapping transcripts on the same strand (Eichhorn et al., 2014). The genome index also included sequences of the quantification spikes and the common portion of the poly(A)-tail length standards. The sequences that identified each RNA standard (the last 20 nt of each standard sequence, Table S3) were not aligned using STAR. Instead, the unix program grep (v2.16) was used to determine which reads matched each standard (allowing no mismatches), and these reads were added to the aligned reads from the STAR output. Tags corresponding to annotated 3′ UTRs of mRNAs were identified using bedtools (v2.26.0), and if the poly(A)-tail read (read 2) contained a stretch of $\geq$ 10 T residues (the reverse complement of the tail) in an 11-nt window within the first 30 nt, this read was carried forward for GHMM analysis. If read 2 failed to satisfy this criterion but began with $\geq$ 4 T residues, the tail length was called based on the number of contiguous T residues at the start of read 2; by definition, these tails were < 10 nt and thus easily determined by direct sequencing.

For each read 2 that was to be input into the GHMM a 'T signal' was first calculated by normalizing the intensity of each channel for each cycle to the average intensity of that channel when reading that base in read 1 and then dividing the T channel by the sum of the other three channels. Sometimes a position in a read would have a value of 0 for all four channels. A read was discarded if it contained more than five such positions. Otherwise, the values for these positions were imputed using the mean of the five non-zero signal values upstream and downstream (ten positions total) of the zero-valued position. A three-state GHMM was then used to decode the sequence of states that occurred in read 2. It consisted of an initiation state (state 1), a poly(A)-tail state (state 2), and a non-poly(A)-tail state (state 3). All reads start in state 1. From state 1 the model can remain in state 1 or transition to state 2. From state 2 the model can either remain in state 2 or transition to state 3. The model was initialized with the following transition probabilities:

from\to	$State_1$	$State_2$	$State_3$
$state_1$	0.001	0.95	0.049
$State_2$	0.001	0.95	0.049
$State_3$	0.001	0.001	0.998

The initial emissions were Gaussian distributions with means of 100, 1, and −1 and variances of 1, 0.25 and 0.25, respectively. In general, the emission Gaussians for the model corresponded to the logarithm of the calculated T signal at each sequenced base in read 2. The initial state probabilities were 0.998, 0.001, and 0.001 for states 1, 2 and 3, respectively.

After initializing the model, unsupervised training was performed on 10,000 randomly selected PAL-seq tags, and then the trained model was used to decode all tags, with the number of state 2 cycles reporting the poly(A)-tail length for a tag. Only genes with ≥ 50 poly(A)-tail length measurements were considered for analyses involving mean poly(A)-tail lengths.

Analysis of PAL-Seq ss-Ligation Data

To account for mRNAs with very short tails or extensive terminal modifications, we implemented a version of PAL-seq that did not use splinted ligation. Tail lengths from these ss-ligation datasets, acquired for steady-state samples from both cell lines, were determined using a modified version of the PAL-seq analysis pipeline written for python3. The T-signal in this pipeline was modified to allow more accurate detection of mRNAs lacking tails. Instead of normalizing the intensity of each channel for each cycle to the average intensity of that channel when reading that base in read 1, the intensity of each channel was normalized to the average intensity of the channels for the other three bases in read 1. The intensity of the T channel was then divided by the sum of the other channel intensities to calculate the T signal, and tails were called using the hmmlearn package (v0.2.0). Tags representing short tails, including short tails that ended with many non-A residues, were identified as those for which read 1 and read 2 mapped to the same mRNA 3′ UTR (usually ~4% of the tags). Tail lengths for these tags were called without the use of the GHMM. Instead, their tail lengths were determined by string matching, allowing any number of untemplated U residues but no more than two G or C residues to precede the A stretch. Tags not identified as representing short-tails were analyzed using the GHMM, excluding from further analysis occasional outliers determined by the GHMM to have tails ≤ 8 nt.

Most of the tags that had either only a very short tail or no tail did not correspond to mRNA cleavage-and-polyadenylation sites. Therefore, to be carried forward in our analysis, short-tailed tags were required to have a 3′-most genome mapping position (as determined from read 1 but requiring that read 2 also map uniquely to the same 3′ UTR) that fell within a 10 nt window of a PAL-seq–annotated cleavage-and-polyadenylation site.

Although the single-stranded ligation protocol provided the opportunity to account for mRNAs with very short or highly modified tails, examination of the recovery of internal standards indicated that tags representing longer tails (≥ 100 nt) were not as well recovered in the datasets in which we implemented ss ligation. Therefore, for steady-state samples from each cell line, we generated composite tail-length distributions in which the ss-ligation dataset contributed to the distribution of tails < 50 nt, and the splinted-ligation dataset contributed to the distribution of tails ≥ 50 nt. For example, *Slc38a2* had 635 standard PAL-seq tags, 169 of which (~27%) had tails < 50 nt, and this same gene had 703 ss-ligation PAL-seq tags, 393 of which (~56%) had tails < 50 nt. The composite tail-length distribution replaced the 169 short-tailed splinted-ligation PAL-seq tags with the 393 short-tailed ss-ligation PAL-seq tags, normalizing the latter cohort by a scaling factor. This scaling factor was determined from the ratio of the counts of the splinted-ligation tags with tail lengths between 30–70 nt (135 tags) to the counts of the corresponding tags in the ss-ligation dataset (153 tags).

3′ end annotations were generated from PAL-seq tags with tails ≥ 11 nt, using an algorithm previously developed for data from poly(A)-position profiling by sequencing (3P-seq) (Jan et al., 2011). Each PAL-seq read 1 that mapped (with at least 1 nt of overlap) to an annotated 3′ UTR (Eichhorn et al., 2014) was compiled by the genomic coordinate of its 3′-UTR nucleotide closest to the tail. The genomic coordinate with the most mapped reads was annotated as a 3′ end. All reads within 10 nt of this end (a 21 nt window) were assigned to this end and removed from subsequent consideration. This process was repeated until there were no remaining 3′ UTR-mapped reads. For each gene, the 3′ end annotations were used in subsequent analyses if they accounted for ≥ 10% of the 3′ UTR-mapping reads for that gene.

Documentation and code to calculate and analyze T signals and determine tail lengths are available for both the splinted-ligation and ss-ligation pipelines at https://github.com/kslin/PAL-seq.

TAIL-Seq

The 2 h time-interval TAIL-seq sample used for comparison with PAL-seq was prepared using the same library cDNA as was used for PAL-seq v2 libraries, but amplifying the library using different primers (Table S3). The first read of TAIL-seq involved sequencing the 3′ UTR from the gene body toward the tail, with the sequencing primer annealing to sequences added with the 5′ adaptor. This 5′ adaptor was an equimolar mixture of four sequences with different numbers of nucleotides in between the primer binding site and the insert (Table S3) to ensure that highly abundant sequences (such as rRNA fragments) did not cause a large portion of the flow cell to fluoresce in a single channel. Amplification and purification were as for PAL-seq v2. Samples were sequenced with either a paired-end 50-by-250 run (2 h time-interval sample) using a HiSeq 2500 operating in normal mode using a v3 kit. Other Illumina

sequencing chemistries (including v1, v2, and v4 kits run in rapid and normal modes) did not yield accurate tail-length measurements when used in paired-end mode. Analysis was as described for PAL-seq v2, except a five-state GHMM was used (Chang et al., 2014) to accommodate the difference in the nature of the T-signal output imparted by the different mode of sequencing. The five states were an initiation state, a poly(A) state, a poly(A) transition state, a non-poly(A) transition state, and a non-poly(A) state.

RNA-Seq

Fragmented poly(A)-selected RNAs were supplemented with three short quantification standards (Table S3), and then ligated to adapters, reverse-transcribed, and amplified to prepare the RNA-seq and ribosome-profiling libraries, respectively (Subtelny et al., 2014). These libraries were sequenced on an Illumina HiSeq 2500. For all RNA-seq data, only reads mapping to ORFs of annotated gene models (Eichhorn et al., 2014) were considered, excluding the first 50 nt of each ORF. The latter requirement which was implemented to match ribosome-profiling data of a concurrent study examining the effects of miRNAs (Eisen et al., 2020). A cutoff of $\geq$ 10 reads per million mapped reads (RPM) was applied to each gene in each sample.

Calculation of mRNA Half-Lives

Half-lives were estimated independently from both RNA-seq data and PAL-seq tag abundance. Prior to half-life fitting, mRNA abundances were normalized across time intervals based on the quantification standards added to each sample prior to library preparation.

Half-lives associated with the mRNAs from each gene j were determined by fitting to the equation

$$m_j(t_i) = \delta \frac{\alpha_j}{\beta_j}\left(1 - e^{-\beta_j(t_i - t_{off})}\right) \tag{1}$$

in the case of the continuous-labeling experiment, or to the equation

$$m_j(t_i) = \frac{\alpha_j}{\beta_j} e^{-\beta_j t_i} + c_j \tag{2}$$

in the case of the transcriptional shutoff experiment, where $m_j(t_i)$ is the expression of mRNA j at time t, α_j is the rate constant for mRNA production, β_j is the rate constant for mRNA degradation, t_{off} is a global time offset, δ is a global scaling parameter to adjust the steady-state time point, and c_j is a baseline for the final expression of each gene in the transcriptional-shutoff experiment. Because the quantification standards were not applicable to the steady-state samples (as these samples did not undergo 5EU purification), the steady-state samples were normalized by a globally fitted constant (setting t_i to 100 h for this time interval).

Because the half-life fitting for the continuous-labeling experiment required the global parameters t_{off} and δ, half-lives for all genes needed to be fit simultaneously. Accordingly, we minimized the least-squares error loss function, $L_2(p)$:

$$L_2(p) = \sum_i^I \sum_j^J \left[\ln(m_{ij}(p)) - \ln(y_{ij})\right]^2, \tag{3}$$

for the simulated number of normalized tags at time point i for gene j, m_{ij}, and the observed number, y_{ij}. The total number of time points and genes are denoted by I and J, respectively. L_2 depends on the parameters p = (α_1, α_2, …, α_J, β_1, β_2, …, β_J, t_{off}, and δ). The optimization for α_j, β_j, t_{off}, and δ was performed using the "L-BFGS-B" method in the *optim* function in R.

To increase the efficiency of the optimization, we also calculated and implemented the analytical gradient of the model-and-loss function. This gradient computed the quantity (dL_2/dp) which, when passed to the optimizer, decreased the number of iterations required to minimize the loss. This quantity was computed for each of the parameters as follows:

$$\frac{dL_2}{d\alpha_j} = \sum_i^I \zeta \frac{\delta}{\beta_j}\left(1 - e^{-\beta_j(t_i - t_{off})}\right) \tag{4.1}$$

$$\frac{dL_2}{d\beta_j} = \sum_i^I \zeta \left(\left(\frac{\alpha_j}{\beta_j^2}\right) e^{-\beta_j(t_i - t_{off})} - \left(\frac{\alpha_j}{\beta_j^2}\right) + \left(\frac{\alpha_j}{\beta_j}\right) t_i e^{-\beta_j(t_i - t_{off})} - \left(\frac{\alpha_j}{\beta_j}\right) t_{off} e^{-\beta_j(t_i - t_{off})} \right)(\delta) \tag{4.2}$$

$$\frac{dL_2}{dt_{off}} = -\sum_i^I \sum_j^J \zeta \delta \alpha_j e^{-\beta_j(t_i - t_{off})}, \tag{4.3}$$

$$\frac{dL_2}{d\delta} = \sum_i^I \sum_j^J \zeta \frac{\alpha_j}{\beta_j}\left(1 - e^{-\beta_j(t_i - t_{off})}\right), \tag{4.4}$$

where ζ is the first component of the derivative of the loss function

$$\zeta = 2\left(\ln\left(\frac{\delta\alpha_j}{\beta_j}\left(1 - e^{-\beta_j(t_i - t_{off})}\right)\right) - \ln(y_{ij})\right)\frac{\beta_j}{\delta\alpha_j(1 - e^{-\beta_j(t_i - t_{off})})}. \quad (5.1)$$

δ is constrained such that its value is 1 for non-steady–state time points and only fit at steady state (i.e., fit when $t_i = t_{ss}$ and 1 otherwise).

The range of rate constants fit to this exponential model and the subsequent deadenylation model was bounded to reflect the lack of confidence in values of and differences between extreme outliers. Half-life values were bounded to fall between 6 min and 100 h, deadenylation rate constants were truncated to fall between 0.03 and 30 nt/min, decay rate constants at 20 nt were truncated to fall between 0.003 and 3 min^{-1}, and production rate constants were truncated to fall between 10^{-8} and 10^{-5} min^{-1}.

Model of mRNA Metabolism

The model of mRNA production, deadenylation, and decapping (decay) was a system of differential equations

$$\frac{dA_l}{dt} = k_0 - (k_1 + k_2)A_l \quad (6.1)$$

$$\frac{dA_{l-1}}{dt} = k_0 + k_1A_l - (k_1 + k_2)A_{l-1} \quad (6.2)$$

$$\frac{dA_{l-2}}{dt} = k_0 + k_1A_{l-1} - (k_1 + k_2)A_{l-2} \quad (6.3)$$

$$\frac{dA_0}{dt} = k_0 + k_1(A_1) - k_2(A_0), \quad (6.4)$$

where A_l is an mRNA with tail length l, and k_0, k_1, and k_2 are rate constants that describe the production, deadenylation and decay rates, respectively. The final deadenylation product (A_0) has a deadenylation rate constant of zero, as it has no tail. The rate constants k_0 and k_2 are themselves functions of tail length (l), specified by the respective negative binomial and logistic functions

$$k_0(l) = \frac{\alpha\Gamma(v_p + l)}{l!\Gamma(v_p)}\left(\frac{m_p}{v_p + m_p}\right)^l\left(\frac{v_p}{v_p + m_p}\right)^{v_p} \quad (7.1)$$

$$k_2(l) = \frac{\beta}{\left(1 + e^{-\frac{l - m_d}{v_d}}\right)}, \quad (7.2)$$

where the parameters α, β, v_p, m_p, m_d, v_d, are fitted parameters. The parameters α and β are scaling terms for production and decay distributions, respectively. The parameters m_p and m_d describe the expected value of those distributions, and v_p and v_d describe the spread.

Equations (6) were re-written as a linear, time-invariant (LTI) system (Dahleh et al., 2004)

$$\dot{x} = \begin{bmatrix} -k_1 - k_2 & 0 & \cdots & 0 & 0 \\ k_1 & -k_1 - k_2 & & & 0 \\ \vdots & \ddots & & \ddots & \vdots \\ 0 & & & -k_1 - k_2 & 0 \\ 0 & 0 & \cdots & k_1 & -k_2 \end{bmatrix} x(t) + \begin{bmatrix} k_o \\ k_0 \\ \vdots \\ k_0 \\ k_0 \end{bmatrix}, \quad (8)$$

or, more succinctly, as

$$\dot{x} = Cx(t) + D, \quad (9)$$

where the coefficient matrix, C, is specified by the coefficients of the differential Equations (6), and the source vector D is specified by the production rate. C is a 251 × 251 matrix, whereas D, $x(t)$, and $\dot{x}$ are 251 × 1 vectors. Although k_0 and k_2 do not depend on time, they do depend on tail length (Equation 7). In the case of the continuous-labeling experiment, $x(t = 0) = 0$. The transcriptional-shutoff experiment begins with $x(t = -1\ \text{h}) = 0$, but $x(t = 0)$ is determined by the values of the system after 1 h of simulation.

Equation 9 has the analytical solution

$$x(t) = C(e^{ct} - I)D, \tag{10}$$

where I is the identity matrix and e^{ct} is the matrix exponential of the coefficient matrix scaled by time. Both this analytical solution and numerical integrators (which do not require an analytical solution) can be used to compute the result. We found that numerical stability and computational efficiency were optimal when using the LSODE solver with parameters set for a banded Jacobian matrix in the *deSolve* package (v1.21) of R, with the model written in C and dynamically loaded into R. Increasing the number of allowed tail-length states from 250 to 300 had little effect on the resulting fitted rate constants but greatly increased computation time.

The model yielded abundances for each tail-length isoform at each time interval, using seven parameters for each gene, three of which were shared across all of the genes (Table S2). From these abundances, the residual sum of squares was computed from the corresponding standard-normalized PAL-seq datasets. Although the 250 nt tail length was modeled, measurements for this length were not available from PAL-seq v2, and thus were excluded from the fitting. Likewise, tail-lengths < 20 were modeled for all time intervals, but because the abundance of tail lengths < 20 nt was only available for steady state, these lengths were excluded from fitting all but the steady-state interval. As a result, for the continuous-labeling experiment using cell line 1, parameters for each gene were fit to 1400 data points (230 tail lengths × 5 time intervals + 250 for the steady-state), and for the experiment using the cell line 2, parameters for each gene were fit to 1170 data points. The optimization was performed using the "L-BFGS-B" method in the *optim* function of R, or, in the case of the global fitting, using the "L-BFGS-B" method in the *NLopt* package (v1.0.4) of R.

A simple L_2 loss function skewed the fits to the time intervals that had larger values. A common solution to this problem is to fit to log-transformed values, but because our data were sparse, with many tail-length positions having zero tags, pseudo-counting to allow log-space fitting resulted in poor fits. Therefore, residuals were variance weighted using the loss function

$$L_2(p) = \sum_{i}^{I} \sum_{j}^{J} \sum_{k}^{K} \frac{\left(x_{ijk}(p) - y_{ijk}\right)^2}{\mathrm{Var}(y_i)}, \tag{11}$$

where i, j, and k are the time-interval, gene, and tail length with I, J and K as the maximal values of time-intervals, genes, and tail lengths, and $\mathrm{Var}(y_i)$ is the variance of the dataset from time-interval i.

The model is constrained by the 0-tail-length species, which builds up when decay is slow with respect to deadenylation. Such a buildup was observed in the steady-state tail-length distribution of short-lived mRNAs but occurred primarily between 0 and 20 nucleotides (Figure 6C). Because of this discrepancy, a composite residual was calculated for the model and the data. Abundances for tails < 20 nt were averaged and this average was used to replace the abundances for each tail length < 20 nt for the steady-state data. In addition, when comparing the associated short tails from the data and the model, the residuals for tails < 20 nt were weighted by either 6- or 5-fold (cell lines 1 and 2, respectively) to account for opting not to fit to measurements for tails < 20 nt in the non-steady–state samples.

As with gene-specific parameters, global parameters v_p, m_d, and v_d were fit using pre-steady-state measurements of tails ranging from 20–249 nt. The composite steady-state tail-length distributions of Figure 2A were also used, which constrained buildup of short-tailed mRNAs. Fitting was performed on subsets of 100 genes (selected randomly without replacement from genes with composite steady-state distributions, yielding 22 and 15 subsets for cell lines 1 and 2, respectively), including v_p, m_d, and v_d in the parameter vector. Median values of the global parameters (Table S1) were then used to fit each gene-specific parameter.

Bootstrap Analysis

Tags in the cell line 1 PAL-seq dataset were resampled 10 times with replacement and assigned to a gene and tail length based on a multinomial probability distribution generated from the counts for each tail length in the original dataset. These resampled datasets were then used for background subtraction, global parameter determination, and model fitting.

Background Subtraction for PAL-Seq Data

Although the efficacy of the 5EU purification enabled efficient enrichment of labeled RNAs at short time intervals (Eisen et al., 2020), we also modeled and corrected for residual background caused by non-specific binding of the unlabeled RNA to the streptavidin beads (Figure S2F).

We designed our background model under the assumption that the background in the time courses stems primarily from the capture of a fixed amount of non-5EU labeled mRNA during the 5EU purification. Accordingly, we subtracted a fraction (0.3%) of the steady-state data from each continuous-labeling dataset. This fraction of input sample was chosen such that at 40 min long-lived genes (half-life $\geq$ 8 h) had no mRNAs with tail lengths $\lessapprox$100 nt on average, but short-lived genes (half-life $\leq$ 30 min) were unaffected (Figure S2F). Likewise, we subtracted standard-normalized time-interval–matched input data from each transcriptional-inhibition dataset, as actD influenced which unlabeled cellular mRNAs were available to contribute to the background. The fraction of each input sample to subtract was chosen such that at 0 h long-lived genes (half-life $\geq$ 8 h) had no mRNAs with tail lengths $\lessapprox$100 nt on average, but short-lived genes (half-life $\leq$ 30 min) were unaffected. Genes were included in the final background-subtracted set only if the sum of their background-subtracted tag counts was $\geq$ 50 tags.

After background subtraction, PAL-seq datasets were scaled to each time interval by matching the total number of background-subtracted tags for all genes at all tail lengths to the total number of tags for all genes for the corresponding time interval in the RNA-seq data. The scaled PAL-seq data were then used to compute half-lives for each gene, scaling the steady-state sample using a globally fitted constant.

ActD Treatment

Cell line 2 was cultured as in the continuous-labeling experiments. We prepared 2, 2, 2, 3, and 4 500 cm^2 plates for the 0, 1, 3, 7 and 15 h time intervals, respectively. 5EU (400 μM final) was added to each plate (with one non-5EU plate prepared in parallel), and after 1 h actD (5 μg/mL final concentration, Sigma-Aldrich) was added. Cells were harvested as described for the continuous-labeling experiments, except that a quantitative spike RNA containing 5EU and corresponding to the chloramphenicol-resistance gene sequence (Table S3) was added to the lysis buffer at a concentration of 0.57 ng/mL, or 2 ng/plate. This RNA was prepared using an *in vitro* transcription reaction as above, with a 5EUTP-to-UTP ratio of 1:20.

QUANTIFICATION AND STATISTICAL ANALYSIS

Graphs were generated and statistical analyses were performed using R (R Core Team, 2019). Statistical parameters including the value of n, statistical test, and statistical significance (p value) are reported in the figures and their legends. No statistical methods were used to predetermine sample size.

DATA AND CODE AVAILABILITY

Raw and processed RNA-seq, PAL-seq, and TAIL-seq read data are available at the GEO, accession number GEO: GSE134660. Code for configuring an Illumina HiSeq 2500 machine for PAL-seq and for calculation of tail lengths from PAL-seq or TAIL-seq data are available at https://github.com/kslin/PAL-seq. Code for fitting kinetic models of abundance and tail length is available at https://github.com/timeisen/DynamicsOfCytoplasmicMrnaMetabolism.